

Fluid inerter-based vibration control of multi-modal structures subjected to vertical vibration

Miriam Chillemi^a, Thomas Furtmüller^a, Christoph Adam^{a,*}, Antonina Pirrotta^b

^a Universität Innsbruck, Unit of Applied Mechanics, Technikerstr. 13, 6020 Innsbruck, Austria

^b University of Palermo, Department of Engineering, viale delle Scienze, 90128 Palermo, Italy

ARTICLE INFO

Keywords:

Cross-laminated timber (CLT) panel
Experimental testing
Fluid inerter
Nonlinearities
Structural control
Vertical vibration

ABSTRACT

The so-called inerter is an attracting device that offers a solution to the goal of realizing or improving structural control devices with high mass ratios while avoiding the undesirable increase in dead load. The research presented here focuses on evaluating the performance of a fluid inerter in mitigating vertical vibrations of structures that exhibit multi-modal behavior, such as plates. First, a numerical study based on previous experimental data investigates the properties of the connection between the inerter and the structure to be controlled. Considering that a flexible connection has been shown to introduce a linearization effect, while a rigid connection of the inerter to the controlled structure can achieve significant displacement reductions, the influence of these two connection types over different inertance ratios is analyzed. To evaluate the practical suitability of the flexible connection to reduce the inherent nonlinear effects associated with the device, a novel application of the fluid inerter for vibration control in multi-modal structures is presented, exemplified by a cross-laminated timber panel, and compares its control performance with that of a conventional Tuned Mass Damper (TMD). This provides insight into the effectiveness of the inerter in controlling vertical vibrations. In addition, optimization procedures are employed to determine connection parameters that enhance the effectiveness of both the TMD and the inerter in mitigating vertical vibrations.

1. Introduction

Due to its remarkable mechanical properties, the so-called inerter has received considerable attention in both academia and industry over the last two decades. The term “inerter”, coined by M. Smith in the early 2000s [1], refers to a mechanical two-ports device capable of generating an internal force proportional to the relative acceleration between its two terminals. The intuition of such a device stems from the need to complement the similar dynamics between mechanical and electrical systems [2]. However, the fulfillment of the force-current analogy is only one of the inerter's features, and its properties go beyond this theoretical comparison. In fact, the inerter has been already widely employed in several engineering fields [3]. Originally, it was used in the automotive sector under the code-name “J-damper” to improve the mechanical grip in the suspension systems of racing cars [4]. Later, inerters have been used for novel applications or to solve classical problems in other fields such as aerospace engineering, ocean engineering, vibration energy harvesting and especially civil engineering [5–7]. Here, these devices have been implemented in railway vehicle suspensions, as well as for vibration absorption in buildings, bridges and cables [8–11].

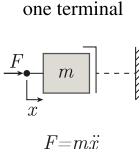
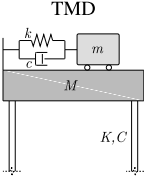
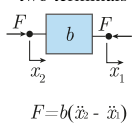
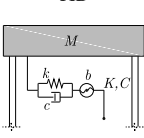
Especially in civil engineer practice, the inerter's large apparent mass property can be more advantageous than in other fields, as it can be effectively utilized in structural control applications [12]. Generally, structural control involves a series of measures aimed at mitigating displacement amplitudes in vibration-prone systems [13]. Within this field, a distinction can be made between passive, active, semi-active and hybrid devices [14]. The preference for passive devices for civil engineering applications arises from their independence from an external power source, making vibration control systems more cost-effective and robust [15]. Therefore, one of the motivations for proposing the inerter as a passive vibration control device is to replace or improve conventional mass–spring–damper configurations whose performance are severely limited by their design [16]. In fact, inerters have been widely studied in recent years as stand-alone vibration control devices or coupled with other mass-dependent devices [17].

To better illustrate the effect of a simple lumped mass m and the apparent mass induced by the inertance b in structural control, Table 1 shows two applications of such inertia components. The combination of the mass m with a spring–dashpot–damper element yields the conventional Tuned Mass Damper (TMD) [18]. Analogously, the inertance

* Corresponding author.

E-mail address: christoph.adam@uibk.ac.at (C. Adam).

Table 1
Comparison between mass and inerter [43].

Inertia component	Symbol	Diagram	Application
Mass	m [kg]		
Inerter	b [kg]		

b , generated by an inerter, can replace the mass m , resulting in the so-called Tuned Inerter Damper (TID) [19]. The significant advantage of the TID over the TMD is that b is not a physical mass and therefore does not impose any additional load to the structure to be controlled. While, for practical reasons, the TMD mass ratio μ , i.e., the ratio between the auxiliary mass m and the mass of the structure to be controlled M , should not exceed 5% [20], the inertance ratio $\beta = \frac{b}{M}$ can be profitably larger, since the actual mass of the device is orders of magnitude smaller than the inertance generated [21]. As an alternative, the control effect of a TMD can be improved by adding an inerter rather than replacing the mass m , forming the so-called Tuned Mass Damper Inerter (TMDI) [22]. This also works with other passive control devices such as the Tuned Liquid Damper [23], Tuned Liquid Column Dampers [24], and Base Isolation System (BIS) [25] that provide with the addition of an inerter such as various the Tuned Viscous Mass Damper [26], Rotational Inertia Double-Tuned Mass Damper [27], Tuned Liquid Column Damper Inerter (TLCDIs) [28], BIS in combination with TMDI [29] or with TLCDI [30], etc.

However, while for the mass the governing law (Newton's second law) is assumed to be exact, the inerter is a technical device that must be manufactured [31–33]. This means that the linear mass amplification effect of the inerter only exists approximately due to deviations from linear behavior such as backlash [34], nonlinear compliance [35], friction [36], fluid compressibility [37], nonlaminar flow [38], cavitation [39], etc. As shown in previous studies [40], for efficient dynamic simulations using a linearization procedure, a linear mathematical model can be found that preserves the intrinsic characteristic of a real (nonlinear) inerter prototype. As an alternative to mathematical linearization, the undesirable nonlinear characteristics of a real inerter can be eliminated by connecting the device to the structure to be controlled via a spring–dashpot–damper element [41]. In [41] it has been shown that the inclusion of this element creates a mechanical buffer that can reduce the nonlinear effects associated with the real mechanical inerter throughout the entire frequency range [42]. On the other hand, experiments [40] have shown that the control performance achieved by the inerter is significant when it is rigidly coupled to the system to be controlled, i.e. when there is no buffer in between. Therefore, it can be concluded that the connection between the inerter and the structure to be controlled plays an important role in both the linearization effect and the control performance.

On this basis, the present paper aims to further investigate the influence of the connection for inerter-based structural control arrangements. Specifically, the nonlinear mechanical model of a real fluid inerter developed in previous studies by the same authors [44] is employed to numerically evaluate the difference of the effect of (i) a *rigid connection* and (ii) a *flexible connection*. While the *rigid connection* involves only the inerter as a stand-alone control device, establishing

a *flexible connection* between the inerter and the system to be controlled transforms the whole arrangement into that of a TID [19]. This peculiarity opens the way for additional analyses and comparisons. Therefore, the flexible connection is analyzed from the point of view of control performance, taking into account different inertance ratios with a view to practical applications and comparisons with possible conventional control devices. In addition, the linearization effect of such connection is examined and compared with the outcomes of standard statistical linearization tools applied to the nonlinear equations of motion of the real device.

To extend and consolidate the findings of previous studies [39,40], this paper presents a new experimental campaign with the fluid inerter prototype. Specifically, the inerter is applied to a cross-laminated timber (CLT) panel in order to evaluate its effectiveness in reducing excessive displacements due to vertical excitation, while, for the first time, experimentally validating the numerical outcomes related to the connection conditions. The choice of a CLT panel for the tests is motivated by the intention to experimentally assess a slender structure that is inherently more prone to vibration. In this way, it is possible to assess, for the first time, experimentally the effective vertical vibration control offered by a fluid inerter, while investigating the actual efficacy of the flexible connection in mitigating the inherent nonlinear effects associated with the device. The CLT plate used in the tests is designed as a scaled structure that exhibits dynamic behavior comparable to that of a real structure analyzed in previous studies [45]. This type of structure shows multi-mode vibration behavior characteristic of plates. This feature allows the exploration of various aspects of control performance, including practical considerations in device design and comparisons with traditional alternatives. In fact, unlike [46], this work experimentally examines the effect of fluid inerter control on a multi-modal structure, including considerations regarding the linearization effect that the connection may exhibit.

Further, [47] assesses the control performance of inerter-based suppression configurations applied to harmonically excited laminated composite plates. In contrast to [47], this paper's evaluation of the effectiveness of a specific type of manufactured inerter is experimentally driven and supplemented by numerical simulations.

Direct comparisons with other control devices are made, including the examination of connection design parameters. On this basis, considerations regarding the inadequacy of traditional optimization formulas, due to the multi-modal nature of the structure to be controlled, pave the way for different procedures to obtain optimal values of well-recognized traditional devices such as TMDs. Hence, optimization procedures are implemented in order to derive connection parameters suitable to improve the effectiveness of the control devices in reducing vibrations in CLT panels.

The paper is organized as follows: In Section 3 the control performance of a *rigid connection* between inerter and structure to be controlled is evaluated and a linearization technique for the existing nonlinear effects is proposed. Furthermore, the influence of a *flexible connection* on the nonlinearities of the real system is analyzed for different parameter setups. In Section 4, an experimental application with a real inerter connected to a CLT plate is presented. A comparative study with a conventional TMD is carried out as well as the optimization of the connection parameters.

2. Considered fluid inerter and mechanical modeling

As outlined in the introduction, the adoption of a very simple model of an inerter such as the one illustrated in Table 1, would lead to an oversimplified definition of the device. This is especially true for fluid inerters, which are prone to a number of nonlinear effects [44]. Moreover, contrary to the mechanical model presented in Table 1, numerical analyses indicated that one of the inerter terminals must be immovably fixed to achieve maximum mass amplification effect [48].

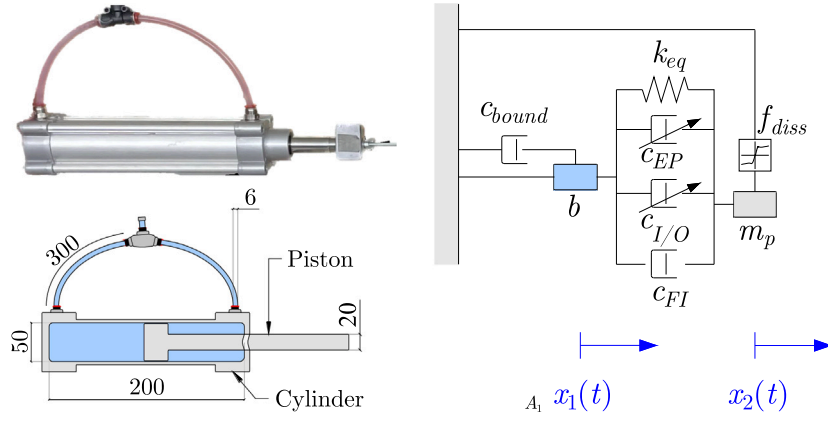


Fig. 1. Photo, sketch and mechanical model of the real fluid inerter [40] (dimensions in millimeters).

Therefore, this section presents the mechanical model and parameters of a real fluid inerter. The model is derived from experiments performed in previous studies [40,44] and is repeated here for ease of reference. The prototype tested at the Unit of Applied Mechanics, Universität Innsbruck, consists of a hydraulic cylinder in which a piston can move back and forth (Fig. 1). An external pipe with a considerably smaller diameter is attached to the cylinder and water is employed as the working fluid. The inertial effect produced by the device is therefore due to the simple working principle of the water flowing in the external pipe. As a result to comparative studies, the mechanical model of such a prototype was successfully retrieved [44] as shown in Fig. 1. It consists of a two degrees-of-freedom (DOFs) system with piston mass m_p and inertance b . A dissipation force element f_{diss} serves to model the friction arising between the piston rod and the cylinder [49] and is defined as [50]

$$f_{diss}(\dot{x}_2) = \left(F_d \tanh \left(4 \frac{|\dot{x}_2|}{v_s} \right) + (F_s - F_d) \frac{\frac{|\dot{x}_2|}{v_s}}{\left(\frac{1}{4} \left(\frac{|\dot{x}_2|}{v_s} \right)^2 + \frac{3}{4} \right)^2} \right) \text{sgn}(\dot{x}_2) + r\dot{x}_2 \quad (1)$$

where F_s and F_d are the static and dynamic friction, respectively, v_s is Stribeck velocity and r is the viscous damping coefficient modeling the contact between lubricated surfaces. The inertance element b (displacement x_1) is grounded by means of the dash-pot damper c_{bound} . On the other side, it is connected to the piston mass m_p (displacement x_2) via a series of springs, which are collectively labeled with the variable k_{eq} and arranged in parallel to the dash-pot dampers denoted by c_{EP} , $c_{I/O}$ and c_{FI} . The spring models the compressibility of the fluid in conjunction with the effect of the air trapped in the system while c_{EP} and $c_{I/O}$ are nonlinear elements that take into account dissipative effects such as pressure losses in the external pipe and at the inlet and outlet of the cylinder. The dash-pot damper c_{FI} captures an additional viscous damping effect due to the presence of the air [44]. All the parameters relevant to the mechanical model are listed in Table 2.

In contrast to previous experimental analyses on fluid inerters [51], the mechanical properties of the device are explicitly considered in this study. This approach results in a more accurate definition of the dissipation force and nonlinearities arising from dissipative effects [40]. Moreover, in order to evaluate the performance of the real fluid inerter when employed as passive control device, the aforementioned mechanical model is analyzed in combination with a system whose vibrations need to be mitigated. In this study, for the first time, a careful examination is made of the connection between the inerter and the target system to be controlled, as well as various design parameters. Specifically, the system chosen to be controlled is a single-DOF

Table 2
Parameters of the real fluid inerter [40].

Parameter	Symbol	Value
Static friction force [N]	F_s	21.14
Dynamic friction force [N]	F_d	15.07
Stribeck velocity [m/s]	v_s	0.0362
Viscous damping coefficient [Ns/m]	r	104.5
Equivalent spring stiffness [N/m]	k_{eq}	3.6×10^4
Ext. pipe damping coefficient [Ns/m]	c_{EP}	1.82×10^3
Inlet/outlet damping coefficient [Ns/m]	$c_{I/O}$	4.21×10^3
Fluid damping coefficient [Ns/m]	c_{FI}	447.65
Boundary damping coefficient [Ns/m]	c_{bound}	652.18
Piston mass [kg]	m_p	0.925
Inertance [kg]	b	29

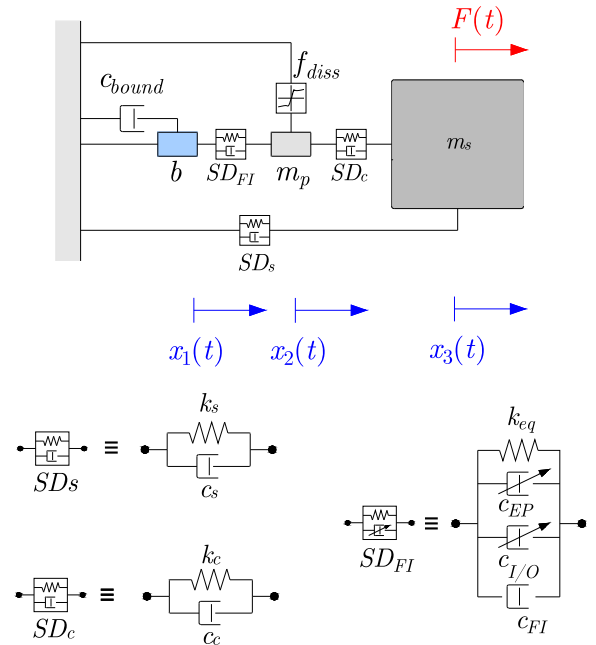


Fig. 2. Mechanical model of the SDOF system controlled by the real fluid inerter (top) and sketches of the visco-elastic elements (bottom).

(SDOF) system with displacement $x_3(t)$, consisting of the main mass m_s grounded by means of the visco-elastic connection element SD_s , which consists of a parallel arrangement of a spring–dashpot–damper component with stiffness k_s and damping c_s . Its natural frequency f_s is set to 2 Hz. Table 3 contains the parameters of this uncontrolled system.

Table 3
Parameters of the uncontrolled system.

Parameter	Symbol	Value
Main mass [kg]	m_s	58/580
Natural frequency [Hz]	f_s	2
Damping ratio [-]	ζ_s	0.03

Coupling of the real fluid inerter (Fig. 1) with the system to be controlled results in the controlled system shown in Fig. 2. The connection between the control unit and the main system can be realized flexible or rigid. In the first case, the Kelvin–Voigt element SD_c is inserted, which consists of a spring-dashpot damper element with stiffness k_c and damping c_c to model a *flexible connection* between the piston of the real fluid inerter and the mass m_s of the main system. Alternatively, the control provided by the real fluid inerter rigidly attached to the uncontrolled system is analyzed considering the extreme case where the spring stiffness k_c of the setup in Fig. 2 is infinitely high so that the displacements x_2 and x_3 coincide. In general, the nonlinear equations of motion of the controlled system depicted in Fig. 2 subjected to the excitation force $F(t)$ can be written as follows [44],

$$\mathbf{M} \ddot{\mathbf{x}} + \mathbf{C} \dot{\mathbf{x}} + \mathbf{K} \mathbf{x} + \mathbf{f}_{nl} = \mathbf{f} \quad (2)$$

with

$$\mathbf{M} = \begin{bmatrix} b & 0 & 0 \\ 0 & m_p & 0 \\ 0 & 0 & m_s \end{bmatrix}, \quad \mathbf{C} = \begin{bmatrix} c_i + c_{bound} & -c_i & 0 \\ -c_i & c_i + c_c & -c_c \\ 0 & -c_c & c_s + c_c \end{bmatrix},$$

$$\mathbf{K} = \begin{bmatrix} k_{eq} & -k_{eq} & 0 \\ -k_{eq} & k_{eq} + k_c & -k_c \\ 0 & -k_c & k_s + k_c \end{bmatrix},$$

$$\mathbf{x} = \begin{Bmatrix} x_1(t) \\ x_2(t) \\ x_3(t) \end{Bmatrix}, \quad \mathbf{f}_{nl} = \begin{Bmatrix} c_{EP}(\dot{x}_2 - \dot{x}_1)^{1.75} + c_{I/O}(\dot{x}_2 - \dot{x}_1)|\dot{x}_2 - \dot{x}_1| \\ f_{diss}(\dot{x}_2) - c_{EP}(\dot{x}_2 - \dot{x}_1)^{1.75} - c_{I/O}(\dot{x}_2 - \dot{x}_1)|\dot{x}_2 - \dot{x}_1| \\ 0 \end{Bmatrix},$$

$$\mathbf{f} = \begin{Bmatrix} 0 \\ 0 \\ F(t) \end{Bmatrix} \quad (3)$$

where a dot over a variable stands for the derivative with respect to time.

3. Linearization for structural control applications

Previous experimental studies [40] have shown that a *rigid connection* between the real fluid inerter and a single DOF oscillator can significantly reduce the displacement of the system to be controlled, but the response is significantly nonlinear. On the other hand, another investigation [41] has revealed that a *flexible connection* can be beneficial to reduce the nonlinear effects of a real mechanical inerter. On this basis, this section presents a numerical analysis aimed at evaluating the properties of the device connection, considering both control performance and the linearization effect of the considered fluid inerter. The excitation force $F(t)$ is chosen as a band-limited white noise excitation with different power spectral densities (PSDs) to evaluate the influence of the type of connection on the nonlinearities of the real fluid inerter for different excitation levels.

3.1. Rigid connection

In order to evaluate the control performance of the coupled system with *rigid connection*, in Fig. 3 the receptance magnitudes $|H(\omega)|$ of the system of Fig. 2 considering $k_c \rightarrow \infty$ (colored solid lines) for different PSDs amplitudes S_0 are set in contrast with the receptance magnitude of the uncontrolled system, which coincides with the case

Table 4
Linearized equivalent damping values for the rigid connection.

S_0 [N ² /Hz]	c_{eq}^{diss} [kg/s]		$c_{eq}^{EP} + c_{eq}^{I/O}$ [kg/s]	
	$\beta = 0.5$	$\beta = 0.05$	$\beta = 0.5$	$\beta = 0.05$
100	1101.4	1760.1	128.4	32.1
500	481.4	1304.1	260.6	64.5
1000	314.1	1031.3	344.6	87.2

of $k_c \rightarrow 0$ (black solid line). Moreover, two different inertance ratios, $\beta = 0.5$ and $\beta = 0.05$, are taken into account. Specifically, an inertance equal to the 50% of the mass of the system to be controlled can be considered as reasonable value to leverage the mass amplification effect of the inerter [52]. On the other hand, $\beta = 0.05$ is the typical value of the mass ratio usually deemed optimal in case of structures controlled by TMD [18]. Therefore, due to the large mass amplification effect that inerters can provide, 5% would result in a rather low value of inertance when employed for such devices. Nevertheless, a system with this small mass ratio is also being investigated in order to enable a fairer comparison between different control devices. The FRFs shown in Fig. 3, are obtained from the simulated time histories of $F(t)$ and $x_3(t)$ applying the *tfestimate* command implemented in MATLAB [53]. To improve the clarity of the results, the frequency f is normalized by the natural frequency f_s of the SDOF oscillator (Table 3). As can be seen, for $\beta = 0.5$ the displacement response of the uncontrolled system is significantly reduced over the entire frequency range, while a lower inertance ratio ($\beta = 0.05$) results in a less effective device, although it is still able to largely reduce the vibrations of the uncontrolled system around the resonance peak. However, as the amplitude of the signal increases, so do the amplitudes of $|H(\omega)|$, revealing the aforementioned nonlinear effects outlined in Eq. (2).

Despite the good performances obtained in the case of *rigid connection*, conventional linear dynamic simulations are preferable and more suitable for numerical studies and for applications in engineering practice. Therefore, the accurate mechanical model retrieved, which captures the actual nonlinear behavior of the system, is replaced in the following by an equivalent linear model. The statistical linearization technique [54] is employed to linearize the nonlinear contributions of Eq. (2), i.e. \mathbf{f}_{nl} . Equivalent damping factors c_{eq} are computed such that the mean square error between the nonlinear and the linearized contribution is minimized with respect to c_{eq} itself [55],

$$E \left[(f(\dot{x}) - c_{eq}\dot{x})^2 \right] = \min_{c_{eq}} \quad (4)$$

where $E[\cdot]$ denotes the expectation operator and $f(\dot{x})$ is a generic nonlinear damping force that depends on the velocity \dot{x} . Specifically, $f(\dot{x})$ corresponds to the nonlinear contributions of \mathbf{f}_{nl} in Eq. (3), namely the friction force and the pressure losses in the external pipe and at the inlet and outlet. Once the minimum is evaluated, the equivalent damping is obtained, recalling that the ensemble average merges with the mean value [56]. The linearized equivalent damping values c_{eq}^{diss} and $c_{eq}^{EP} + c_{eq}^{I/O}$ obtained by means of Eq. (4) are summarized in Table 4.

The linearization effect achieved employing the statistical linearization technique is shown in Figs 4 and 5. Here, the receptance values of the nonlinear real fluid inerter coupled to the uncontrolled system via the *rigid connection* (blue solid line) are compared with those of the linearized fluid inerter (red dashed line) for different excitation amplitudes. The agreement is extremely close for both $\beta = 0.5$ (Fig. 4) and $\beta = 0.05$ (Fig. 5) and for all the excitation levels considered. Therefore, it can be concluded that the statistical linearization technique is able to cope with the problem of nonlinearities that occur when the control device consists of the real inerter rigidly connected to the uncontrolled system.

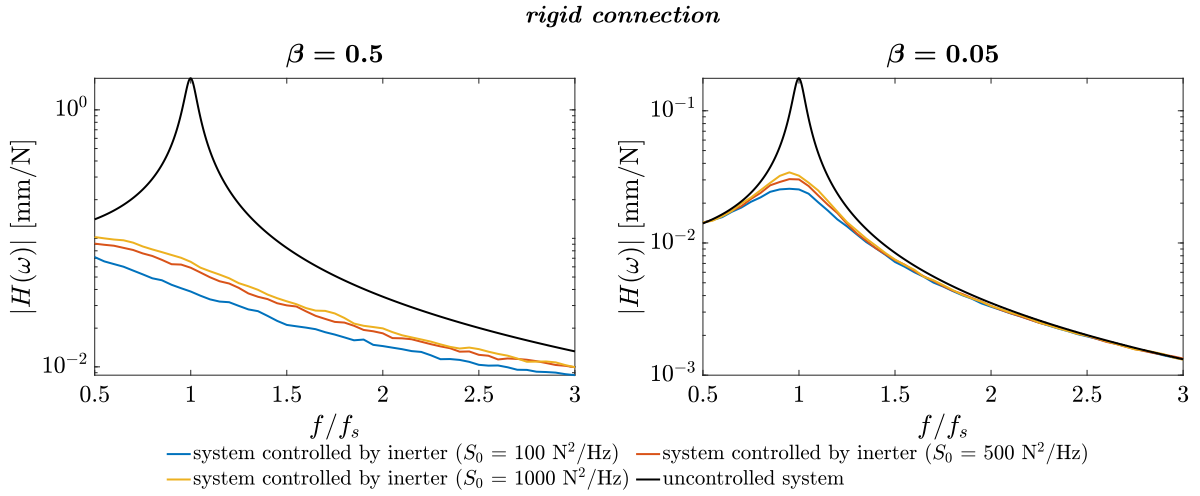


Fig. 3. Receptance magnitudes of the controlled system with rigid connection (colored solid lines) versus the uncontrolled SDOF system (black solid line). (For interpretation of the references to colour in this figure legend, the reader is referred to the web version of this article.)

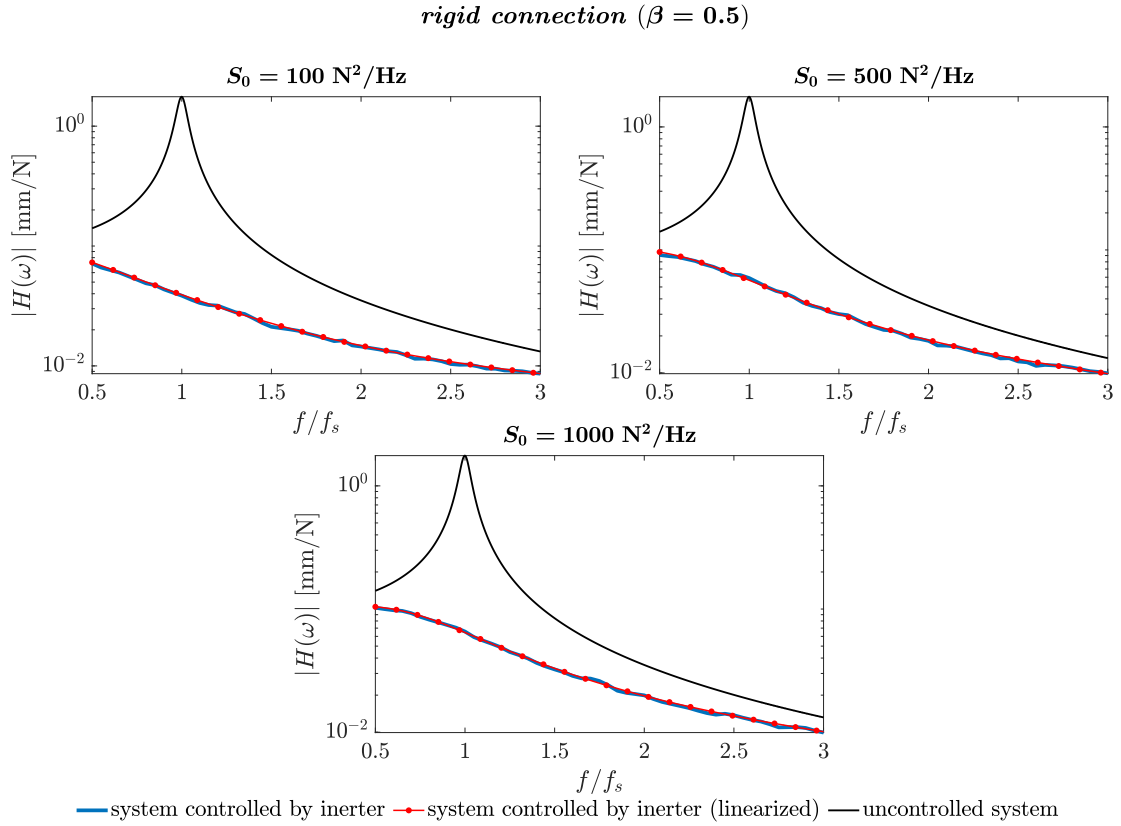


Fig. 4. Receptance magnitudes of the real (blue solid line) and linearized (red solid line with markers) controlled systems with rigid connection versus the uncontrolled SDOF system (black solid line) for $\beta = 0.5$ and different excitation amplitudes. (For interpretation of the references to colour in this figure legend, the reader is referred to the web version of this article.)

3.2. Flexible connection

This section examines the device that is connected to the main system via a *flexible connection*. Although the nonlinear quantities of Eq. (2) are inherent on the system in this case too, an almost linear response behavior is expected according to [41]. It is therefore of great interest to evaluate the effectiveness of this type of coupling in compensating for the non-linearities of the real fluid inerter and in

mitigating the vibrations. Its efficiency can be compared with the case of the *rigid connection* (Fig. 3), recalling that for numerical applications it is possible to eliminate nonlinearities thanks to the statistical linearization technique. In Fig. 6, the receptance magnitudes of the controlled system with *flexible connection* and the uncontrolled system are plotted for different excitation amplitudes and for the two inertance ratios studied. In the first set of results, depicted in colored solid lines,

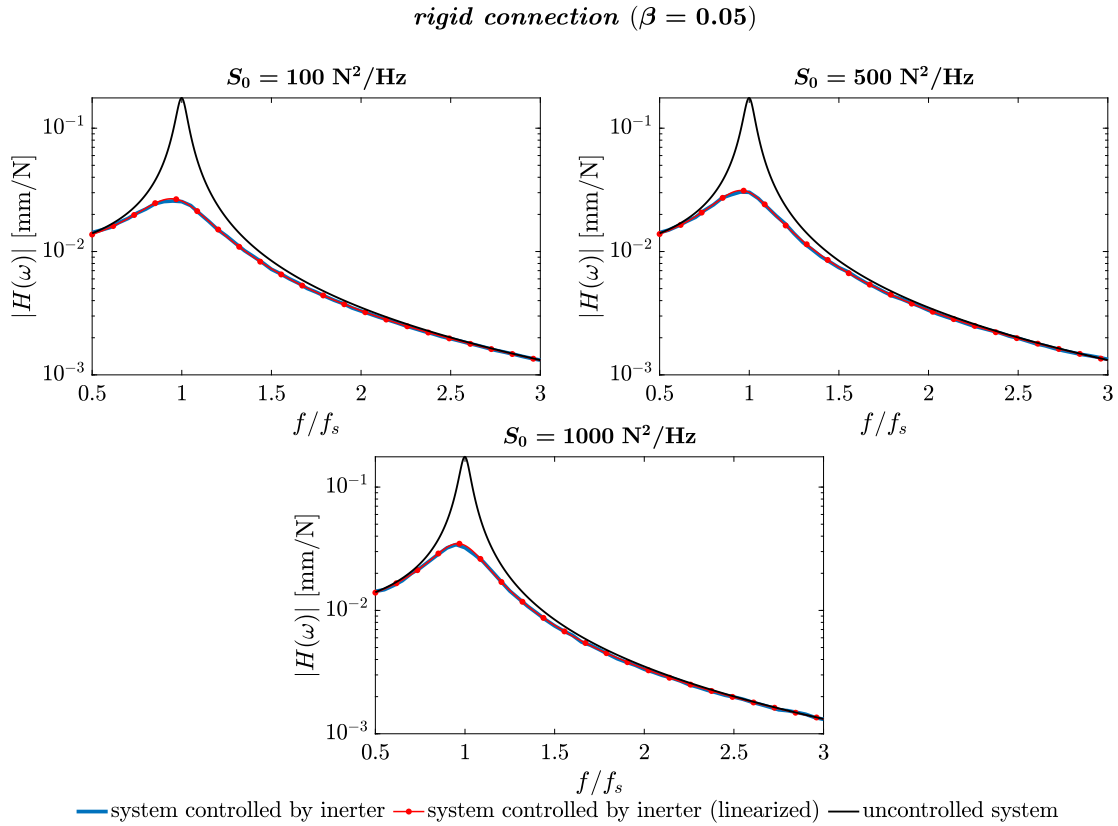


Fig. 5. Receptance magnitudes of the real (solid blue line) and linearized (red solid line with markers) controlled systems with rigid connection versus the uncontrolled SDOF system (black solid line) for $\beta = 0.05$ and different excitation amplitudes. (For interpretation of the references to colour in this figure legend, the reader is referred to the web version of this article.)

k_c and c_c are tuned using the well-known Den Hartog formulas [18],

$$k_c^{DH} = \beta m_s \left(\frac{2\pi f_s}{1 + \beta} \right)^2, \quad c_c^{DH} = 2\beta m_s \left(\frac{3\beta}{8(1 + \beta)} \right)^{\frac{1}{2}} \quad (5)$$

Although Eq. (5) were derived for TMDs [18], it has been shown that they can also be used for the tuning of TIDs [42] and are therefore equally suitable in the case of *flexible connection*. However, the values of k_c and c_c resulting from Eq. (5) represent a rather flexible connection, which does not allow a proper comparison with the experimental results presented in Section 4. For this reason, the receptances of the system with *flexible connection* at an increased value of the stiffness \tilde{k}_c are also shown with dashed colored lines in Fig. 6. Specifically, due to the practical implementation of the *flexible connection* (which will be presented in Section 4), the stiffness resulting from the Den Hartog formulas is increased by a factor of 3, ($\tilde{k}_c = 3k_c^{DH}$).

For both the dashed and solid lines, an overlap of the frequency response functions (FRFs) for different amplitudes suggests that the *flexible connection* can indeed cause a linearization effect. This is more pronounced when the connection given by c_c is quite flexible ($k_c = k_{con}^{DH}$), while for the less flexible connection ($k_c = \tilde{k}_c$) a slight nonlinear behavior is still visible. This result confirms the beneficial effect of the mechanical buffer in reducing the impact of such nonlinear contributions on the global behavior of the system. On the other hand, the control performance in the case of *flexible connection* is severely impaired compared to the case of *rigid connection* (Fig. 3). Although for $\beta = 0.5$ a quite large reduction of the resonance peak of the uncontrolled system can still be observed, this does not apply when the inertance ratio becomes smaller ($\beta = 0.05$). As β decreases, the vibration mitigation effect of the real fluid inerter becomes less important until it reaches almost zero control over the structure when k_c and c_c correspond to the values of Den Hartog's formulas.

4. Application for vibration control in a cross-laminated timber panel

In this section, the results of an experimental campaign to evaluate the control performance of the real fluid inerter in mitigating vertical vibration, together with the linearization effect of the *flexible connection* described in Section 3.2 is presented. In contrast to previous studies [40], the structure to be controlled emulates the dynamic properties, such as natural frequencies, damping and closely spaced modes, of a real structure analyzed in previous studies [45]. Specifically, the scaled system to be controlled in this experimental setup is a CLT panel, resulting in a multi-modal system.

In general, a CLT panel consist of an odd number of boards of sawn wood that are glued together on their side faces so that each layer is aligned perpendicular to the previous one [57]. This results in elements with a high stiffness-to-weight ratio if compared to e.g. reinforced concrete [45]. Such panels are usually assembled into lightweight structures such as floors, walls, ceilings, roofs and generally into building elements that make full use of the quasi one-dimensional load bearing behavior of wood in both directions [58]. However, their slender nature makes timber systems more prone to vibrations. For example, human-induced vibration may affect floor systems and cause discomfort to occupants if one of the natural frequencies occurring is in resonance with that of the human body [59].

4.1. Experimental setup

The CLT panel tested at the Unit of Applied Mechanics, Universität Innsbruck, is shown in Figs. 7 and 8. The four corners of the slab are marked with counterclockwise increasing numbers, as can be seen in the photo of Fig. 7. It consists of a 200,00 × 97,50 cm slab with three

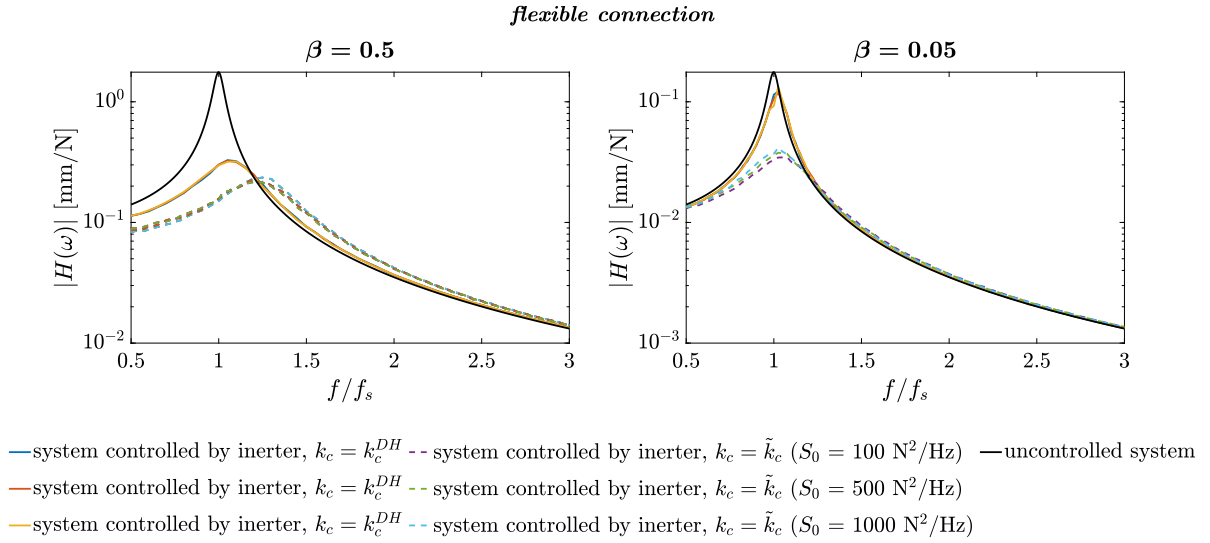


Fig. 6. Receptance magnitudes of the controlled system with flexible connection with $\tilde{k}_{con} = k_{con}^{DH}$ (colored solid lines) and with $\tilde{k}_{con} = k_{con}^{DH}$ (colored dashed lines) versus the uncontrolled SDOF system (black solid line). (For interpretation of the references to colour in this figure legend, the reader is referred to the web version of this article.)

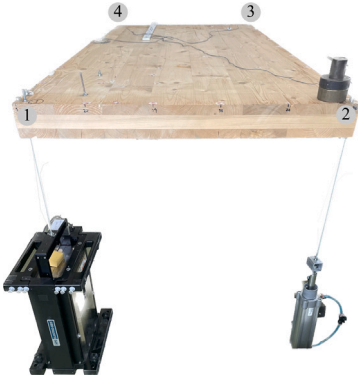


Fig. 7. Photo of the experimental setup of the CLT plate controlled by the fluid inerter.

layers of 3–4–3 cm thickness, with the top layer aligned in parallel to the longitudinal direction of the panel (Fig. 8). The panel is clamped near the corner (4) in an area of approximately 30×70 cm (not visible in the picture). At corner (1), dynamic excitation is provided by an APS 400 Electro-Seis long-stroke shaker from APS Dynamics, Inc., driven by an APS 145 power amplifier. Corner (3) remains free, while corner (2) is connected to the real fluid inerter by an M5 threaded rod. To tune the natural frequencies in a desired frequency range for CLT slabs, a 24 kg mass is placed at the corners (1) and (3) at the bottom of the plate (not visible in the picture), while a 3 kg mass is attached near corner (2).

In order to better visualize the dynamic behavior of the CLT panel, results of a previous experimental modal analysis are presented in Fig. 9. Here, the first three modal shapes of the CLT plate are shown as contour plots. The experimental modal analysis was conducted by placing 6 sensors in a row along the horizontal direction, spaced every 25 cm in the longitudinal direction. This arrangement resulted in a total of 9 rows, corresponding to 54 measurement points. The system identification was carried out by the least squares complex exponential algorithm [60] implemented in the MATLAB command *modalfit*. In general, a frequency range between 10 and 30 Hz can be considered as suitable for the analysis of timber floors [61]. Thus, focusing on the three corner points is sufficient for such a range. Furthermore, in Fig. 9, the mode shapes suggest that corners (1), (2), and (3) are the only critical ones for describing the dynamics of the plate. Based on the

results of this previous study, in the experimental tests, the dynamic response of the CLT slab was recorded with piezoelectric accelerometers of type 4508 from Bruel&Kjaer placed at corners (1), (2) and (3) (Fig. 8). It is important to note that the 3 kg mass added at corner (2) was not considered in the preliminary experimental study. However, the inclusion of this additional mass only marginally affects the natural frequencies of the plate (see Fig. 9 and compare with Table 6). The decision not to repeat the experimental modal analysis for the system with the 3 kg mass is due to the fact that with each test iteration, the drying shrinkage of the timber would inevitably cause slight variations in the parameters. Furthermore, the boundary conditions introduce a slightly nonlinear behavior in the structure, which makes it necessary to determine the parameters by optimization, as will be shown in the following section.

4.2. Mechanical model

To numerically reproduce the experimental results and to evaluate the control performance of the real fluid inerter, the mechanical model of the CLT panel is developed and shown in Fig. 10. The first three DOFs of the system are the displacements $x_1(t)$, $x_2(t)$ and $x_3(t)$ of the corners where the accelerations were recorded. However, in the mechanical model for the plate, these physical coordinates are replaced by the modal displacements $y_1(t)$, $y_2(t)$ and $y_3(t)$ by means of the modal expansion [62]

$$\mathbf{x}(t) = \Phi \mathbf{y}(t) \quad \text{with} \quad \Phi = [\phi_1, \phi_2, \phi_3] \quad (6)$$

as modal matrix Φ composed of three modal vectors ϕ_i , $i = 1, 2, 3$. The latter obtained by solving the eigenvalue problem for the conservative (undamped) system of the CLT plate without shaker and inerter. Applying standard modal analysis, the CLT plate is thus described by three modal equations of motion of the form

$$\ddot{y}_k(t) + 2\zeta_k \omega_k \dot{y}_k(t) + \omega_k^2 y_k(t) = \frac{1}{m_k} \phi_k^T \mathbf{f}(t), \quad k = 1, 2, 3 \quad (7)$$

where ω_k , ζ_k and m_k are the natural circular frequencies, damping ratios and modal masses, while $\mathbf{f}(t) = [F_1(t), F_2(t), 0]^T$ is force applied to the plate as excitation and by the inerter, respectively.

Previous studies [39] have shown that it is both necessary and efficient to consider the electro-mechanical shaker as part of the analyzed system, so that the same excitation voltage signal used during the test can be used in the numerical analyses. This is achieved by modeling the shaker an electromechanical system with 2 DOFs, with

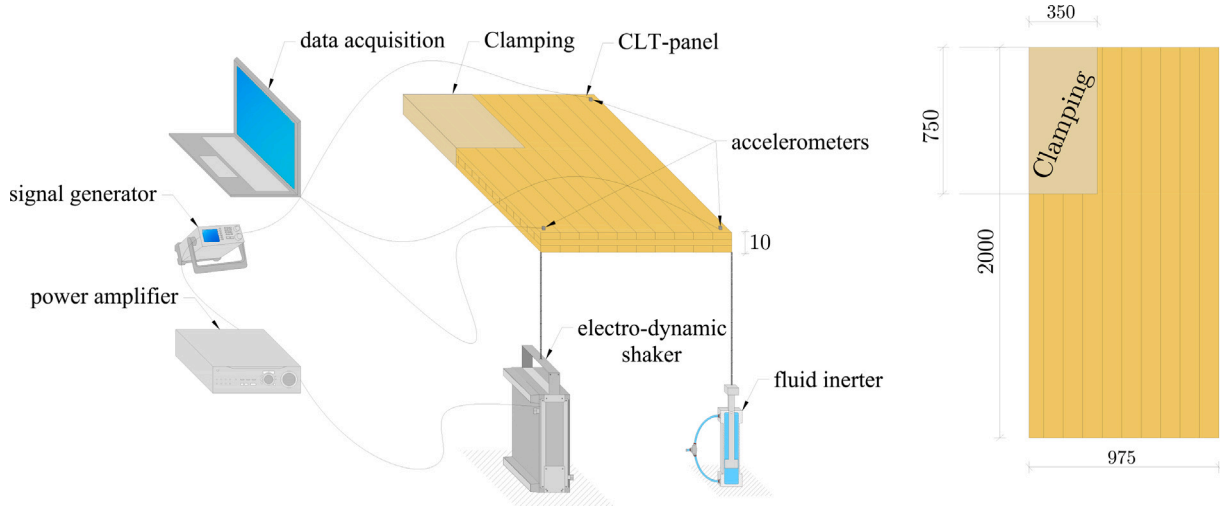


Fig. 8. Sketch of the experimental setup and floor-plan of the CLT plate controlled by the fluid inerter (dimensions in millimeters).

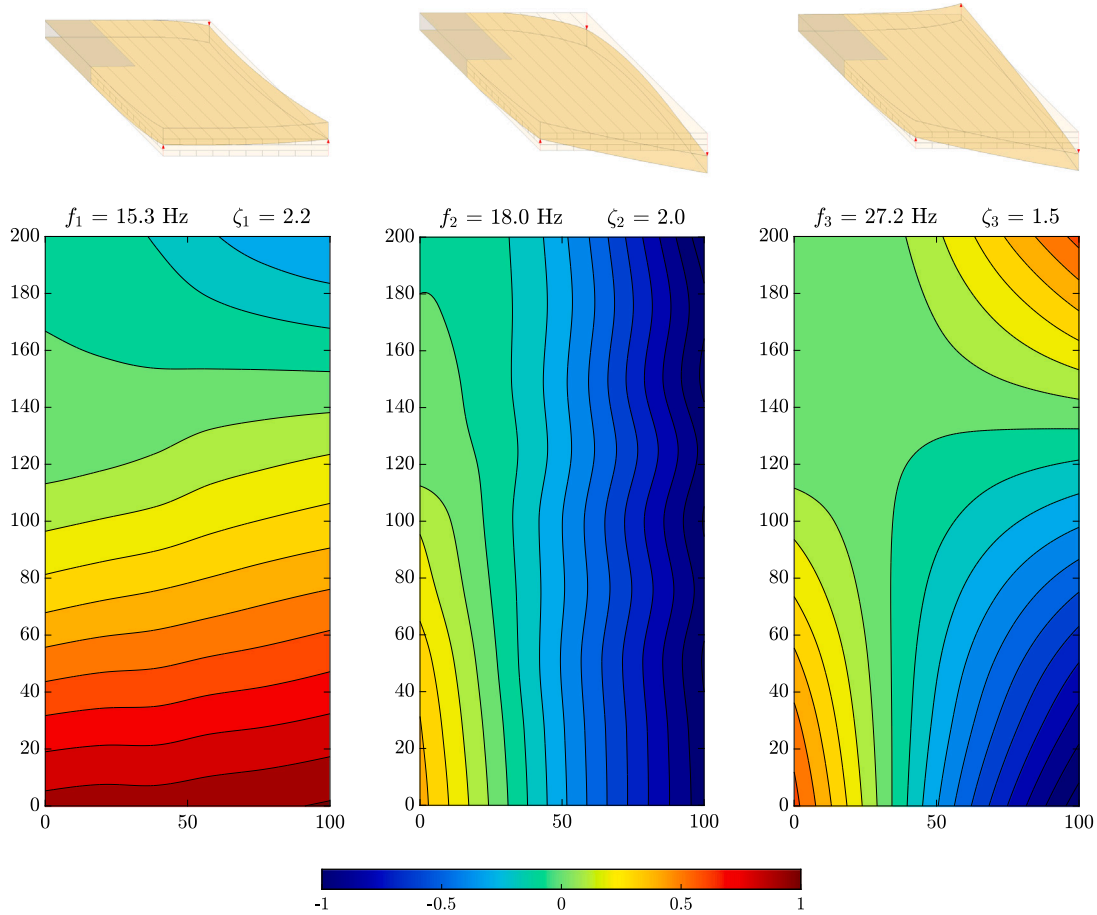


Fig. 9. Modal shapes of the CLT plate in a preliminary study without the 3 kg mass.

the shaker displacement $x_1(t)$ (assumed to be equal to that of corner (1)) and the electrical current $i(t)$ as DOFs [63]. However, to improve the computational efficiency of numerical simulations [39], the electric DOF i is replaced by the electric charge q taking into account the relations $\dot{q}(t) = i(t)$ [64]. The shaker mass m_a is modeled as a lumped mass and grounded via the connector element SD_a , i.e. an spring-dashpot-damper component consisting of a spring of stiffness k_a and the dash-pot damper c_a . Overall, m_a , k_a and c_a represent the mechanical

part of the shaker, while its electrical part consists of R and L , which correspond to the resistance and the inductance of the shaker coil, respectively. Thus, the corner (1) is excited by a force F_1 proportional to the current $i(t)$ through α_1 and the electrical circuit is also excited by an internal voltage $u(t)$ proportional to the velocity of the coil through α_2 . Considering the beneficial linearization effect of a flexible connection, the inerter is simply modeled as a mass b linked to the CLT panel by means of the connector element SD_c and grounded via the dashpot

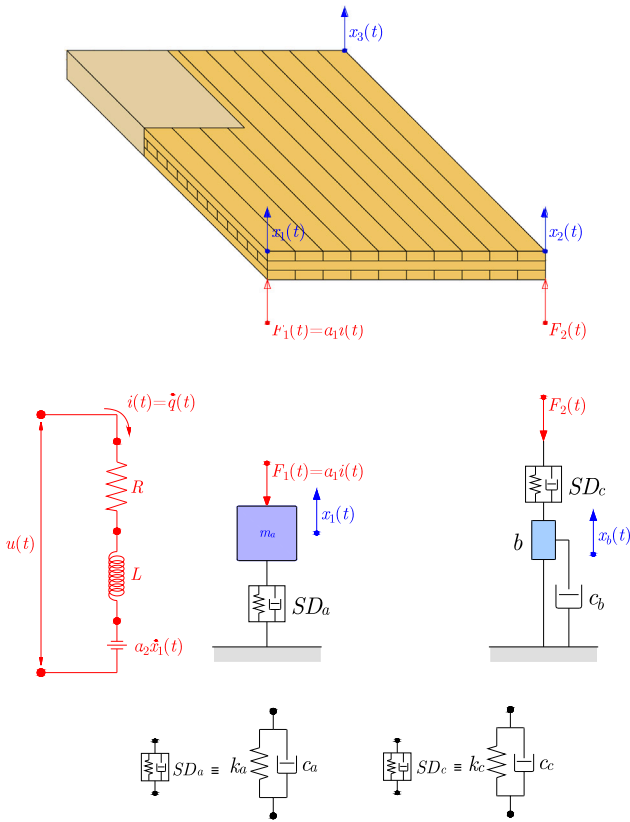


Fig. 10. Mechanical model of the CLT plate controlled by the fluid inerter.

dampers c_b . The inertance produced by the device is thus included in the mass b , whose displacement corresponds to an additional DOF $x_b(t)$, while c_b contains all the (linearized) dissipative and damping effects of the real fluid inerter. Obviously, this is a simplified representation of the inerter compared to the two-DOF system shown in Fig. 1 in Section 2.

A direct implementation of this two-DOFs inerter model with appropriate linearized damping coefficients for the investigated system would require knowledge of the inertance ratio β - which is ambiguous in a multi-modal system - and the excitation level - which, in this case is not applied directly to the inerter but to the CLT plate. Recalling the mechanical model of the controlled system in Fig. 2, SD_c coincides with an spring-dashpot-damper element of stiffness k_c and damping c_c , yielding the *flexible connection* between the fluid inerter and the system to be controlled. Note that the level of stiffness provided by k_c in the experimental setup is comparable to that of \tilde{k}_c in Section 3. Specifically, it is adjusted to three times the stiffness that the connection would have if its parameters were tuned using Den Hartog's formulas (Eq. (5)). As mentioned in the previous section, this level of stiffness should be sufficient to mitigate the nonlinear effects associated with the fluid inerter (Fig. 6). Overall, the mechanical model of the CLT panel, excited by the electro-mechanical shaker and equipped with an inerter, is represented by a linear system with five DOFs in the form

$$\tilde{\mathbf{M}} \ddot{\mathbf{y}}(t) + \tilde{\mathbf{C}} \dot{\mathbf{y}}(t) + \tilde{\mathbf{K}} \mathbf{y}(t) = \tilde{\mathbf{f}}(t) \quad (8)$$

Referring to a more detailed derivation in Appendix, the matrices and vectors of Eq. (8) (see Eqs. (9)–(12) which are given in Box I).

4.3. System identification

In the experimental and numerical tests presented here, the excitation signal chosen is a linear sweep (chirp) with a maximum voltage

amplitude of 1 V, corresponding to a maximum force amplitude of 150 N in a frequency range between 10 and 30 Hz in a period of 60 s. In order to assess the efficiency of the fluid inerter in controlling the CLT panel, it is necessary to identify the uncontrolled system, i.e. the timber plate without the device. In this case, the force $F_2(t)$ in Fig. 10 is zero, hence the forth row and column of Eq. (9),(10),(11) and the fourth row in the vectors of Eq. (12) are omitted, resulting in a four-DOF system. The electro-mechanical properties of the shaker, i.e. R , L , ω_a , ζ_a , α_1 and α_2 are known from previous studies [39], while the remaining unknown values are the modal vectors ϕ_k (normalized to $\phi_{k1} = 1$), the modal masses m_k , circular frequencies ω_k and damping ratios ζ_k with $k = 1, 2, 3$, i.e. 18 parameters.

The latter are identified by optimizing the numerical simulations with respect to the experimental outcomes. Specifically, the sum of the squared error between the experimental and numerical frequency response functions (both magnitude and phase) serves as the objective function. To find the minimum values, the Nelder-Mead optimization algorithm implemented in the MATLAB function *fminsearch* is used [65]. The obtained modal parameters are given in Table 6, while Table 5 lists the physical parameters of the shaker (and of the inerter, as identified in the next step). The numerically obtained FRFs $H_j^{(U)}(\omega)$ based on Eq. (8), expressed in units [m/V] due to the experimental setup with input voltage as excitation, are plotted in Fig. 11 as blue solid lines with markers and contrasted with their experimental counterparts (black solid lines). Specifically, $H_1^{(U)}$, $H_2^{(U)}$ and $H_3^{(U)}$ refer to the displacement response at points 1, 2 and 3, respectively (compare with Fig. 10). Note that the system of equations Eq. (8) yields modal displacements y_1 , y_2 and y_3 due to the input voltage $u(t)$, which must be transformed into physical displacements by Eq. (6). As can be seen, both magnitudes and phases agree very well in all the three DOFs and for the entire frequency range. The close agreement between experimental and numerical curves confirms the adequacy of the mechanical setup employed to model the CLT plate as well as the suitability of the identified parameters (Tables 5 and 6).

Therefore, in the next step the remaining model parameters of the inerter are identified, i.e. the connection parameters k_c and c_c as well as the comprehensive inerter damping ratio c_b , where the inertance $b = 29$ kg is known from previous studies [44]. Employing the same optimization procedure as described above, the parameters given in Table 6 are obtained. Based on this, Fig. 12 shows the comparison between numerical (blue solid lines with markers) and experimental (black solid lines) FRFs of the controlled system for the three DOFs considered. Again, both numerical and experimental results are in good agreement, with notable discrepancies only for the DOF where the inerter is attached (DOF 2). Obviously, the simplification of the fluid inerter in the mechanical model of the controlled system (Fig. 10) leads to a higher level of approximation for this DOF than for the others. Nevertheless, the linearization effect due to the *flexible connection* can be considered as effective, since the simplified linear model proposed does indeed capture the behavior of the structure satisfactorily.

4.4. Control performance

In this section, the influence of the (linearized) parameters of the fluid inerter on the control performance of the CLT plate is investigated. As a comparison, the control performance of one of the most commonly used passive control devices, a conventional TMD with comparable mass-to-inertia ratio, located at corner (2) is also determined. The effective mass for mode k at the DOF to which the respective control devices are attached (i.e. DOF 2) is calculated as follows [66],

$$m_{k2}^{eff} = \frac{m_k}{\varphi_{k2}^2} \quad (13)$$

From this relationship, the effective mass for the first mode of the CLT

$$\tilde{\mathbf{M}} = \begin{bmatrix} \frac{\varphi_{11}^2 m_a}{m_1} + 1 & \frac{\varphi_{21}\varphi_{11}m_a}{m_1} & \frac{\varphi_{31}\varphi_{11}m_a}{m_1} & 0 & 0 \\ \frac{\varphi_{21}\varphi_{11}m_a}{m_2} & \frac{\varphi_{21}^2 m_a}{m_2} + 1 & \frac{\varphi_{31}\varphi_{21}m_a}{m_2} & 0 & 0 \\ \frac{\varphi_{31}\varphi_{11}m_a}{m_3} & \frac{\varphi_{31}\varphi_{21}m_a}{m_3} & \frac{\varphi_{31}^2 m_a}{m_3} + 1 & 0 & 0 \\ 0 & 0 & 0 & b & 0 \\ 0 & 0 & 0 & 0 & L \end{bmatrix} \quad (9)$$

$$\tilde{\mathbf{C}} = \begin{bmatrix} 2\zeta_1\omega_1 + \frac{2\zeta_a\omega_a m_a \varphi_{11}^2}{m_1} + \frac{\varphi_{12}^2 c_c}{m_1} & \frac{2\zeta_a\omega_a m_a \varphi_{11}\varphi_{21}}{m_1} + \frac{\varphi_{12}\varphi_{22}c_c}{m_1} & \frac{2\zeta_a\omega_a m_a \varphi_{11}\varphi_{31}}{m_1} + \frac{\varphi_{12}\varphi_{32}c_c}{m_1} & -\frac{\varphi_{12}c_c}{m_1} & -\frac{\alpha_1\varphi_{11}}{m_1} \\ \frac{2\zeta_a\omega_a m_a \varphi_{21}\varphi_{11}}{m_2} + \frac{\varphi_{22}\varphi_{12}c_c}{m_2} & 2\zeta_2\omega_2 + \frac{2\zeta_a\omega_a m_a \varphi_{21}^2}{m_2} + \frac{\varphi_{22}^2 c_c}{m_2} & \frac{2\zeta_a\omega_a m_a \varphi_{21}\varphi_{31}}{m_2} + \frac{\varphi_{22}\varphi_{32}c_c}{m_2} & -\frac{\varphi_{22}c_c}{m_2} & -\frac{\alpha_1\varphi_{21}}{m_2} \\ \frac{2\zeta_a\omega_a m_a \varphi_{31}\varphi_{11}}{m_3} + \frac{\varphi_{32}\varphi_{12}c_c}{m_3} & \frac{2\zeta_a\omega_a m_a \varphi_{31}\varphi_{21}}{m_3} + \frac{\varphi_{32}\varphi_{22}c_c}{m_3} & 2\zeta_3\omega_3 + \frac{2\zeta_a\omega_a m_a \varphi_{31}^2}{m_3} + \frac{\varphi_{32}^2 c_c}{m_3} & -\frac{\varphi_{32}c_c}{m_3} & -\frac{\alpha_1\varphi_{31}}{m_3} \\ -\varphi_{12}c_c & -\varphi_{22}c_c & -\varphi_{32}c_c & c_c + c_b & 0 \\ \alpha_2\varphi_{11} & \alpha_2\varphi_{21} & \alpha_2\varphi_{31} & 0 & R \end{bmatrix} \quad (10)$$

$$\tilde{\mathbf{K}} = \begin{bmatrix} \frac{\varphi_{11}^2 m_a \omega_a^2}{m_1} + \frac{\varphi_{12}^2 k_c}{m_1} + \omega_1^2 & \frac{\varphi_{11}\varphi_{21}m_a \omega_a^2}{m_1} + \frac{\varphi_{12}\varphi_{22}k_c}{m_1} & \frac{\varphi_{11}\varphi_{31}m_a \omega_a^2}{m_1} + \frac{\varphi_{12}\varphi_{32}k_c}{m_1} & -\frac{\varphi_{12}k_c}{m_1} & 0 \\ \frac{\varphi_{21}\varphi_{11}m_a \omega_a^2}{m_2} + \frac{\varphi_{22}\varphi_{12}k_c}{m_2} & \frac{\varphi_{21}^2 m_a \omega_a^2}{m_2} + \frac{\varphi_{22}^2 k_c}{m_2} + \omega_2^2 & \frac{\varphi_{21}\varphi_{31}m_a \omega_a^2}{m_2} + \frac{\varphi_{22}\varphi_{32}k_c}{m_2} & -\frac{\varphi_{22}k_c}{m_2} & 0 \\ \frac{\varphi_{31}\varphi_{11}m_a \omega_a^2}{m_3} + \frac{\varphi_{32}\varphi_{12}k_c}{m_3} & \frac{\varphi_{31}\varphi_{21}m_a \omega_a^2}{m_3} + \frac{\varphi_{32}\varphi_{22}k_c}{m_3} & \frac{\varphi_{31}^2 m_a \omega_a^2}{m_3} + \frac{\varphi_{32}^2 k_c}{m_3} + \omega_3^2 & -\frac{\varphi_{32}k_c}{m_3} & 0 \\ -\varphi_{12}k_c & -\varphi_{22}k_c & -\varphi_{32}k_c & k_c & 0 \\ 0 & 0 & 0 & 0 & 0 \end{bmatrix} \quad (11)$$

$$\mathbf{y}(t) = \begin{Bmatrix} y_1(t) \\ y_2(t) \\ y_3(t) \\ x_b(t) \\ q(t) \end{Bmatrix}, \quad \tilde{\mathbf{f}}(t) = \begin{Bmatrix} 0 \\ 0 \\ 0 \\ 0 \\ u(t) \end{Bmatrix} \quad (12)$$

Box I.

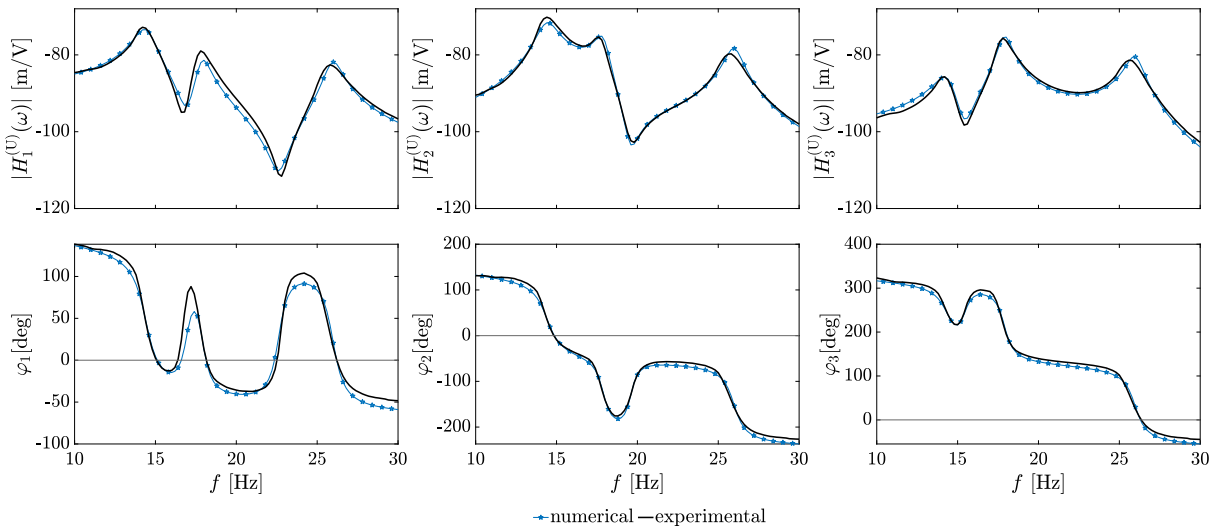


Fig. 11. Numerical (blue solid line with markers) versus experimental (black solid line) FRFs of the uncontrolled CLT plate; magnitudes in dB [re 1 m/V]. (For interpretation of the references to colour in this figure legend, the reader is referred to the web version of this article.)

plate is $m_{12}^{eff} = 28.43$ kg. Given that the physical mass of the inerter is about 2 kg, it seems reasonable to compare its control performance to that of a TMD with the same mass m_d . Consequently, the mass ratio μ

of the TMD, defined as

$$\mu = \frac{m_d}{m_{12}^{eff}}, \quad (14)$$

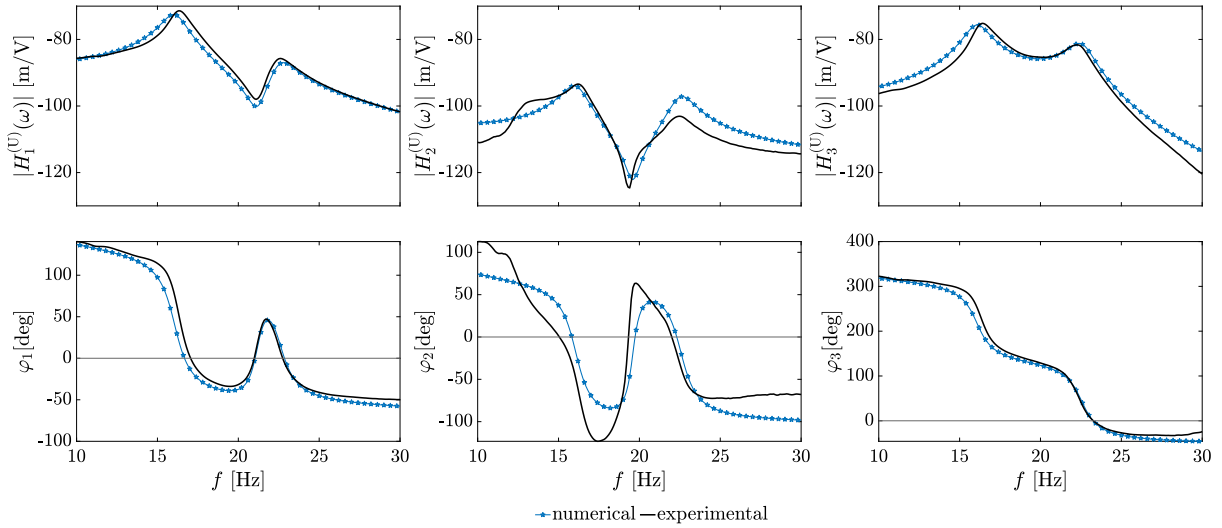


Fig. 12. Numerical (blue solid line with markers) versus experimental (black solid line) FRFs of the fluid inerter-controlled CLT plate; magnitudes in dB [re 1 m/V]. (For interpretation of the references to colour in this figure legend, the reader is referred to the web version of this article.)

Table 5
Physical parameters of the mechanical model.

Parameter	Symbol	Value	Parameter	Symbol	Value
DC Coil Resistance [Ω]	R	1.65	Shaker damping ratio [-]	ζ_a	0.18
Inductance [H]	L	0.019	Inertance [kg]	$b = \rho l \frac{A_1^2}{A_2}$	28.86
Force-current ratio [N/A]	α_1	18.71	Inerter damping [kNs/m]	c_b	5.719
Voltage-velocity ratio [Vm/s]	α_2	15.39	Connection stiffness [kN/m]	k_c	632.98
Armature assembly mass [kg]	m_a	2.70	Connection damping coefficient [Ns/m]	c_c	207.50
Shaker circular frequency [rad/s]	ω_a	31.73			

ρ = density of the working fluid, l = length of the external pipe, A_1 = cross-sectional area of the main cylinder minus the rod, A_2 = cross-sectional area of the external pipe.

Table 6
Modal parameters of the mechanical model.

k	ω_k [rad/s]	f_k [Hz]	ζ_k [-]	m_k [kg]	ϕ_{k1} [-]	ϕ_{k2} [-]	ϕ_{k3} [-]
1	91.86	14.62	0.0334	51.19	1	1.34	-0.19
2	113.14	18.00	0.0209	126.24	1	-1.82	-2.12
3	166.47	26.50	0.0170	48.88	1	-1.37	1.01

corresponds to 0.07.

To tune the parameters of the connection element SD_c between the TMD and the CLT panel with the conventional Den Hartog formulas, Eq. (5) are re-written as follows,

$$k_c^{DH} = \mu m_{12}^{eff} \left(\frac{\omega_1}{1 + \mu} \right)^2, \quad c_c^{DH} = 2\mu m_{12}^{eff} \left(\frac{3\mu}{8(1 + \mu)} \right)^{\frac{1}{2}} \quad (15)$$

Based on the equations of motion Eq. (8), the TMD controlled structure is analyzed by setting $c_b = 0$.

In Fig. 13, the FRF magnitudes $H(\omega)$ of the uncontrolled system (black solid lines), the system controlled by the fluid inerter (blue solid lines) and the system controlled by the TMD (red solid lines) are shown, here expressed in units of m/N, i.e., they represent receptances. To determine them, Eq. (A.3) is used to compute the excitation force $F_1(t)$ based on the solution of the system of equations Eq. (8). As can be seen in the upper right subplot, controlling the CLT panel with the real fluid inerter results in a significant reduction of the displacement $x_2(t)$ (i.e., the displacement of the DOF where the device is attached) over the entire frequency range. Due to the significant mass amplification effect caused by the inerter, a shift in the natural frequencies is observed. While the uncontrolled system has natural frequencies at around 14, 17 and 26 Hz, the system controlled by the real fluid inerter has only two resonance peaks at around 16 and 23 Hz in the considered

frequency range. These natural frequencies coincide with the anti-resonances of the uncontrolled system, which is consistent with the findings of control theory that the open-loop zeros are asymptotic values for the closed-loop poles [67]. This result is further supported by previous outcomes of numerical analyses on inerter-based damping devices attached to a laminated composite plate [47]. Here, the results in terms of kinetic energy also demonstrate a significant change in the dynamic behavior of the plate. However, even in the case of the TMD controlled system, the performance in some frequency ranges is worse than the uncontrolled system at DOFs 1 and 3. Although in this case the counterproductive effect is less pronounced, the TMD is far from achieving such a large reduction of the displacement response as in the case of the system controlled by real fluid inerter at DOF 2.

However, both control devices do not appear to be optimized. In particular, for the TMD the conventional Den Hartog formulas are not suitable in the current application. This is due to the fact that such formulas are tailored to an undamped SDOF oscillator [18], which is a very different system when compared to that of the CLT panel. In [68] it was shown that these formulas are applicable for cases where the natural frequencies are sufficiently far apart from each other so that the TMD only affects the targeted mode of the structure, which is not the case for the CLT plate considered.

In addition to the TMD parameters, the connection parameters of the real fluid inerter could also be subjected to an optimization

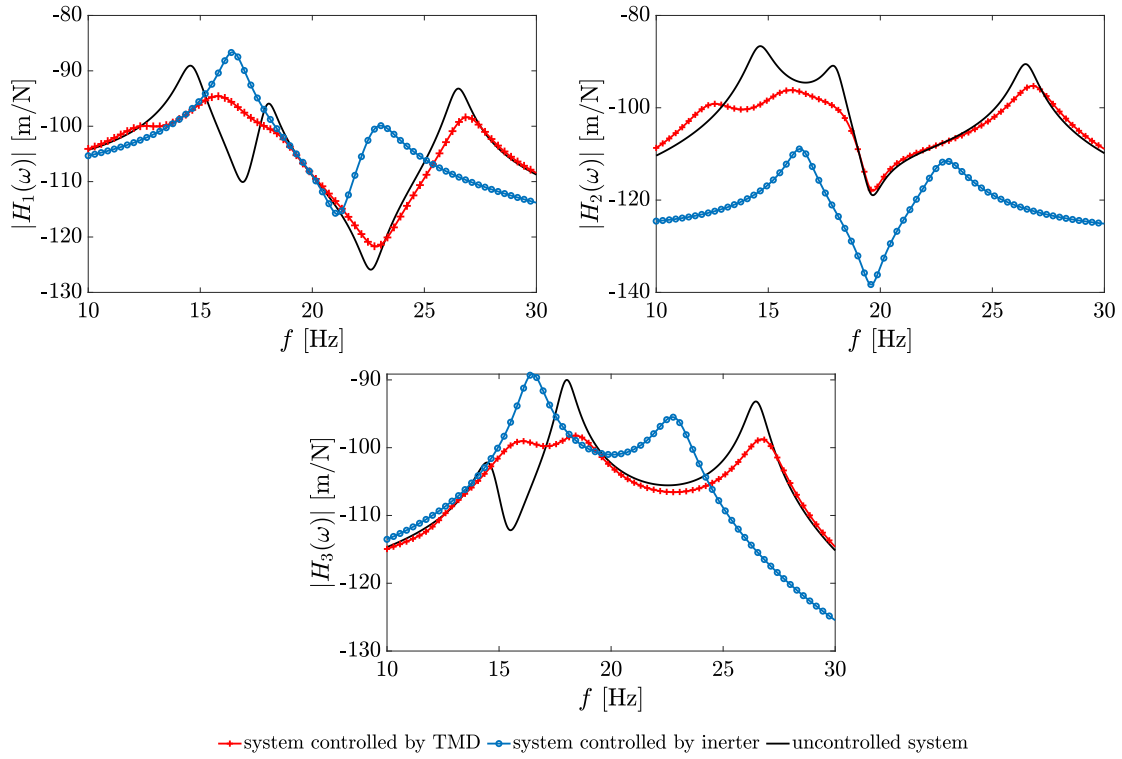


Fig. 13. Receptance magnitudes of the CLT plate controlled by fluid inerter (blue solid line with markers) and TMD (red solid line with markers), respectively, versus uncontrolled CLT plate (black solid line); receptance responses in dB [re 1 m/N]. (For interpretation of the references to colour in this figure legend, the reader is referred to the web version of this article.)

procedure to reduce the magnitude of the resonance peaks at DOFs 1 and 3, although this means some sacrifice of the outstanding control performance at DOF 2. With this in mind, in the next section these parameters are optimized to tune both control devices optimally.

4.5. Optimization of the connection parameters

For the TMD, the parameters are considered optimal if the maximum values of the response magnitudes are the same around the natural frequency under consideration. Therefore, an optimization procedure is employed in which the objective function J_{TMD} is the minimization of the squared difference between the first and the second magnitude peaks of the acceleration response $A_n(\omega)$ (i.e., the ratio of acceleration over an unitary input force in frequency domain) of the system controlled by the TMD, which reads as

$$J_{TMD} = \min \left[\sum_{n=1}^3 \left(|A_n(\omega_2)| - |A_n(\omega_1)| \right)^2 \right] \quad (16)$$

As shown in Fig. 15, using Eq. (16) to optimize the flexible connection parameters, the receptance response of the system controlled by the TMD (red solid line) contains two peaks at the same height at all DOFs and in general the control performance seems to be slightly improved.

In order to optimally tune the parameters of the fluid inerter connection, a compromise between the performance at the three examined positions must be pursued. For the design of timber structures, the use of acceleration is recommended according to [69]. Therefore, minimizing the root mean square (rms) value of the acceleration response of the system is a reasonable choice for this type of application. The objective function for optimizing the real fluid inerter is written as follows,

$$J_{inerter} = \min \left[\sum_{n=1}^3 w_n \sqrt{\frac{1}{T} \int_0^T a_n^2(t) dt} \right] \quad (17)$$

where $a_n(t)$ is the acceleration response squared and averaged over a time period T . In Eq. (17), w_n represents the weighting values for the three individual integral values. Specifically, $w_1 = 2$, $w_2 = 1$ and $w_3 = 2$ were used here. The acceleration time histories are obtained from the inverse Fourier transform of the accelerances $A_n(\omega)$, which are obtained as the acceleration over unit excitation force in the frequency domain at the three positions, which in turn are obtained from the receptances $H_n(\omega)$ by multiplying by $-\omega^2$. This objective function is able to significantly reduce the energy content of the system, as shown in Fig. 14 by comparing the acceleration responses $a_n(t)$.

In addition, Table 7 lists the rms values of the accelerations for the three DOFs considered, comparing the response of the uncontrolled system, the TMD-controlled system and the fluid inerter-controlled system. As can be seen, the TMD-controlled system has a lower acceleration in all DOFs compared to the uncontrolled system. However, its performance is surpassed by the real fluid inerter, whose acceleration values are even lower in all DOFs and especially in accordance with the DOF to which it is attached (DOF 2). More specifically, in Table 8, the decrease in the rms value of the CLT plate acceleration under TMD and fluid inerter control is evident. Notably, a significant reduction in acceleration is observed, particularly for the second and third DOFs.

As a further comparison, Fig. 15 summarizes the control performance of the studied optimized and non-optimized devices compared to the uncontrolled system (black solid line). As mentioned earlier, the control performance of the optimized TMD (yellow solid line with markers) is only slightly improved with respect to the case where Eq. (5) are used (red solid line with markers). On the other hand, the fluid inerter with optimized tuning parameters (green solid line with markers) behaves much better compared to the original experimental setup (blue solid line with markers). However, the better result at DOFs 1 and 3 is achieved at the expense of the control performance at DOF 2. As can be seen in the upper right subplot of Fig. 15, the receptance magnitude of the optimized system controlled by fluid

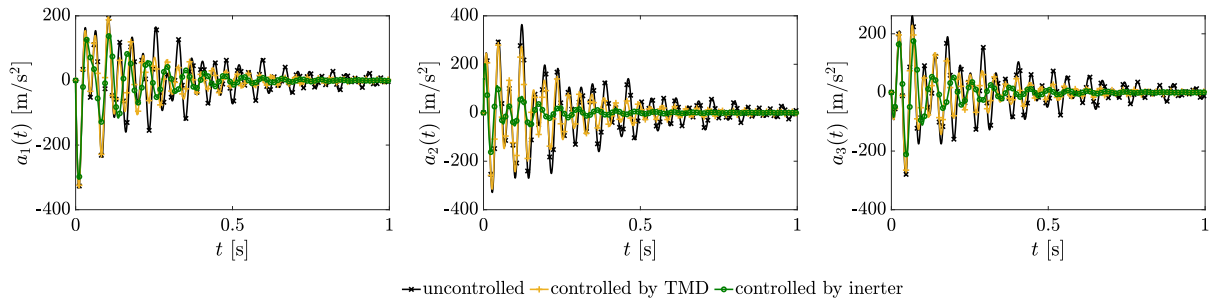


Fig. 14. Acceleration response $a_n(t)$ of the CLT plate controlled by inerter (green solid line with markers), by TMD (yellow solid line with markers) versus uncontrolled system (black solid line). (For interpretation of the references to colour in this figure legend, the reader is referred to the web version of this article.)

Table 7

Root mean square acceleration values of the uncontrolled, TMD-controlled and fluid inerter-controlled CLT plate.

	uncontrolled	controlled by TMD	controlled by fluid inerter
$\text{rms}(a_1)$ [m/s ²]	88.41	83.89	80.43
$\text{rms}(a_2)$ [m/s ²]	73.04	59.25	32.26
$\text{rms}(a_3)$ [m/s ²]	50.70	39.14	29.74

Table 8

Root mean square acceleration reduction values of the CLT plate controlled by TMD and controlled by inerter with respect to the uncontrolled system.

rms acceleration reduction with respect to the uncontrolled system	
controlled by TMD	controlled by fluid inerter
5.1%	8.8%
18.9%	55.8%
22.8%	41.3%

inerter is actually larger than in the case observed experimentally. It is important to note that the performance control at this DOF is still significantly better than the uncontrolled and TMD controlled systems.

5. Conclusions

This study focused on analyzing the effectiveness of a recently developed fluid inerter in reducing vertical vibrations in a cross-laminated timber (CLT) plate, which represents a multi-modal structures. Based on previous experimental results, at first a numerical study was carried out to evaluate the type of connection (rigid vs. flexible) between the inerter and the structure to be controlled. With excitation with different amplitudes, nonlinear effects could be demonstrated. Two inertance ratios (0.5 and 0.05) were considered, to compare the control performance of the fluid inerter with that of the conventional Tuned Mass Dampers (TMD). In addition, an experimental study was carried out in which a CLT plate was equipped with a prototype fluid inerter. Previous experimental simulations performed on a single degree-of-freedom (SDOF) system revealed nonlinear effects in such a device. In response to this observation, the size of the test rig was increased to explore the control performance for a much heavier system with more complex dynamic behavior. Moreover, the fluid inerter was exploited to control the vertical vibrations a multi-modal structure, such as a CLT plate, introducing a more complex scenario compared to the simpler SDOF structure. Such an experimental campaign also allowed to evaluate the linearization effect of the *flexible connection* studied numerically. To this end, the CLT panel was subjected to a linear sweep (chirp) excitation in a frequency range between 10 and 30 Hz. Once the system was identified, the control performance of the fluid inerter in reducing the vertical displacements of the plate was numerically compared with that of a conventional TMD. Optimal tuning parameters were sought for both the fluid inerter and, for comparison, the

conventional TMD. For the inerter, an objective function focused on minimizing the kinetic energy of the system was employed. While, for the TMD, an optimization procedure was implemented to reduce the discrepancy in receptance magnitude between the first two peaks. To sum up, the following conclusions can be inferred:

- When the connection between the fluid inerter and the structure is rigid, a significant reduction in the displacement response can be achieved. However, nonlinear behavior was observed, requiring additional mathematical linearization for further dynamic simulations.
- On the other hand, the use of a flexible connection, as suggested in previous studies, significantly reduces the deviation from linear behavior, eventually vanishing completely for very flexible links. However, this linearization effect comes at the expense of the performance, which, although still good for higher inertance ratios, is less effective than in the case of a rigid connection.
- In the experimental study, significant reductions in displacement were observed for the degree-of-freedom (DOF) where the inerter was attached. However, the efficiency of the inerter was significantly reduced for other DOFs within the structure examined. The level of reduction by the inerter could not be achieved by a TMD. Parameter tuning based on Den Hartog's formulas proved to be suboptimal due to the multi-modal nature of the CLT plate.
- Despite optimization, the TMD could not exceed the efficiency of its original setup due to inherent design limitations. In contrast, after optimization, the fluid inerter also shows superior vibration mitigation effect on the other DOFs at the expense of the remarkable performance achieved at DOF where the inerter is applied.

Future work may include the exploitation of the fluid inerter for larger structural control applications, as its exceptional performance makes it suitable for even heavier structures. This approach will make it easier to elucidate a clearer performance advantage of the inerter over other traditional control devices, such as TMDs. Further investigations may include an experimental study in which the connection between the system to be controlled and the CLT has the optimal parameters identified in this study. Finally, numerical simulations may contribute to a more comprehensive analysis of the optimal design of TMD parameters when employed to control structures whose natural frequencies are closely spaced.

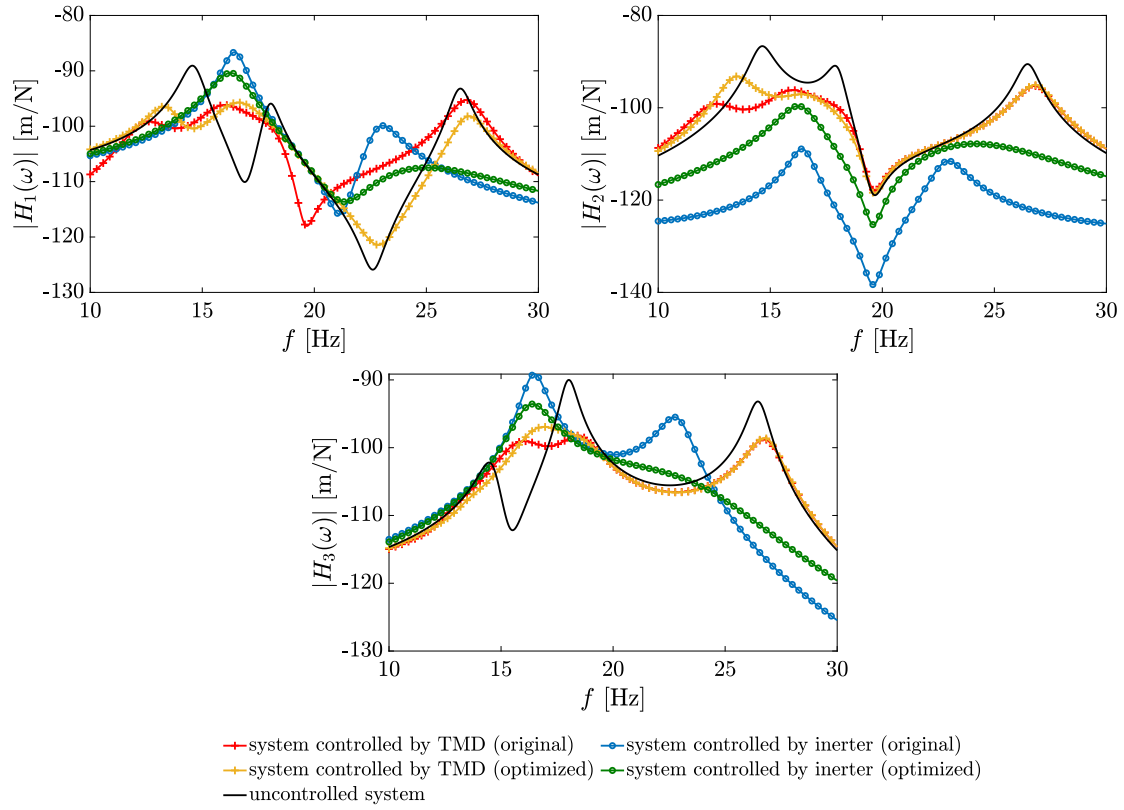


Fig. 15. Receptance magnitudes of the optimized TMD-controlled system (yellow solid line with markers), the non-optimized TMD-controlled system (red solid line with markers), optimized fluid inerter-controlled system (green solid line with markers) and no-optimized fluid inerter-controlled CLT plate (blue solid line with markers) versus uncontrolled CLT plate (black solid line); receptance responses in dB [re 1 m/N]. (For interpretation of the references to colour in this figure legend, the reader is referred to the web version of this article.)

CRedit authorship contribution statement

Miriam Chillemi: Writing – review & editing, Writing – original draft, Visualization, Validation, Software, Methodology, Investigation, Formal analysis, Conceptualization. **Thomas Furthmüller:** Writing – review & editing, Validation, Supervision, Methodology, Investigation, Conceptualization. **Christoph Adam:** Writing – review & editing, Supervision, Project administration, Funding acquisition, Conceptualization. **Antonina Pirrotta:** Writing – review & editing, Conceptualization.

Declaration of competing interest

The authors declare that they have no known competing financial interests or personal relationships that could have appeared to influence the work reported in this paper.

Data availability

The data that has been used is confidential.

Acknowledgments

This project has received funding from the European Union's Horizon 2020 research and innovation programme under the Marie Skłodowska-Curie grant agreement No 847476. The views and opinions expressed herein do not necessarily reflect those of the European Commission.

Appendix. Derivation of equations of motion Eq. (8)

As outlined in Section 4.2, for the CLT panel a modal expansion considering three modes is taken into account. Eqs. (7) serve as starting point, where subsequently $F_1(t)$ and $F_2(t)$ are specified. Considering the electro-dynamic shaker as shown in Fig. 10 as two DOF system, the equations of motion can be written as

$$\begin{aligned} m_a \ddot{x}_1(t) + c_a \dot{x}_1(t) + k_a x_1(t) - \alpha_1 \dot{q}(t) &= -F_1(t) \\ L \ddot{q}(t) + R \dot{q}(t) + \alpha_2 \dot{x}_1(t) &= u(t) \end{aligned} \quad (\text{A.1})$$

Dividing the first equation by the shaker mass m_a and applying the modal transformation of Eq. (6) for $x_1(t)$ the following equations are obtained,

$$\begin{aligned} \sum_{k=1}^3 \left(\phi_{k1} \ddot{y}_k(t) \right) + 2\zeta_a \omega_a \sum_{k=1}^3 \left(\phi_{k1} \dot{y}_k(t) \right) + \omega_a^2 \sum_{k=1}^3 \left(\phi_{k1} y_k(t) \right) \\ = \frac{1}{m_a} (\alpha_1 \dot{q}(t) - F_1(t)) \\ L \ddot{q}(t) + R \dot{q}(t) + \alpha_2 \sum_{k=1}^3 \left(\phi_{k1} \dot{y}_k(t) \right) = u(t) \end{aligned} \quad (\text{A.2})$$

From this,

$$F_1(t) = \alpha_1 \dot{q}(t) - m_a \left[\left(\sum_{k=1}^3 \phi_{k1} \ddot{y}_k(t) \right) + 2\zeta_a \omega_a \sum_{k=1}^3 \left(\phi_{k1} \dot{y}_k(t) \right) + \omega_a^2 \sum_{k=1}^3 \left(\phi_{k1} y_k(t) \right) \right] \quad (\text{A.3})$$

can be inserted in Eq. (8). Considering the linearized model shown in Fig. 10 for the fluid inerter, the two equations of motion read as

$$\begin{aligned} b \ddot{x}_b(t) + c_b \dot{x}_b(t) - c_c (\dot{x}_2(t) - \dot{x}_b(t)) - k_c (x_2(t) - x_b(t)) &= 0 \\ c_c (\dot{x}_2(t) - \dot{x}_b(t)) + k_c (x_2(t) - x_b(t)) &= -F_2(t) \end{aligned} \quad (\text{A.4})$$

Introducing again the transformation of Eq. (6) for $x_2(t)$, Eq. (A.4) can be recast as

$$b\ddot{x}_b(t) + c_b\dot{x}_b(t) - c_c \left[\sum_{k=1}^3 \left(\phi_{k2}\dot{y}_k(t) \right) - \dot{x}_b \right] - k_c \left[\sum_{k=1}^3 \left(\phi_{k2}y_k(t) \right) - x_b \right] = 0 \quad (\text{A.5})$$

$$c_c \left[\sum_{k=1}^3 \left(\phi_{k2}\dot{y}_k(t) \right) - \dot{x}_b \right] + k_c \left[\sum_{k=1}^3 \left(\phi_{k2}y_k(t) \right) - x_b \right] = -F_2(t)$$

Hence, the force $F_2(t)$ can be written as follows,

$$F_2(t) = -c_c \left[\sum_{k=1}^3 \left(\phi_{k2}\dot{y}_k(t) \right) - \dot{x}_b \right] - k_c \left[\sum_{k=1}^3 \left(\phi_{k2}y_k(t) \right) - x_b \right] \quad (\text{A.6})$$

and is inserted in Eq. (8). Together with the first equation in Eq. (A.4) and the second equation in Eq. (A.2), the five-DOF system as described by the matrices in Eqs. (9), (10) and (11) is obtained.

References

- [1] Smith M. Synthesis of mechanical networks: the inerter. *IEEE Trans Automat Control* 2002;47(10):1648–62. <http://dx.doi.org/10.1109/TAC.2002.803532>.
- [2] Chen MZ, Papageorgiou C, Scheibe F, Wang F-c, Smith MC. The missing mechanical circuit element. *IEEE Circuits Syst Mag* 2009;9(1):10–26. <http://dx.doi.org/10.1109/MCAS.2008.931738>.
- [3] Ma R, Bi K, Hao H. Inerter-based structural vibration control: A state-of-the-art review. *Eng Struct* 2021;243:112655. <http://dx.doi.org/10.1016/j.engstruct.2021.112655>.
- [4] Smith MC. The inerter: A retrospective. *Ann Rev Control Robot Auton Syst* 2020;3(1):361–91. <http://dx.doi.org/10.1146/annurev-control-053018-023917>.
- [5] Li Y, Jiang JZ, Neild S. Inerter-based configurations for main-landing-gear shimmy suppression. *J Aircr* 2017;54(2):684–93. <http://dx.doi.org/10.2514/1.C033964>.
- [6] Bubbar K, Buckham B. On establishing generalized analytical phase control conditions in two body self-reacting point absorber wave energy converters. *Ocean Eng* 2020;197:106879. <http://dx.doi.org/10.1016/j.oceaneng.2019.106879>.
- [7] Masnata C, Di Matteo A, Adam C, Pirrotta A. Smart structures through non-traditional design of tuned mass damper inerter for higher control of base isolated systems. *Mech Res Commun* 2020;105:103513. <http://dx.doi.org/10.1016/j.mechrescom.2020.103513>.
- [8] Wang F-C, Liao M-K, Liao B-H, Su W-J, Chan H-A. The performance improvements of train suspension systems with mechanical networks employing inerters. *Veh Syst Dyn* 2009;47(7):805–30.
- [9] Marian L, Giaralis A. Optimal design of a novel tuned mass-damper-inerter (TMDI) passive vibration control configuration for stochastically support-excited structural systems. *Probab Eng Mech* 2014;38:156–64.
- [10] Lazar I, Neild S, Wagg D. Vibration suppression of cables using tuned inerter dampers. *Eng Struct* 2016;122:62–71.
- [11] Gao H, Wang H, Li J, Mao J, Wang Z. Dynamic behavior and damping enhancement of cable with negative stiffness inerter damper. *Int J Mech Sci* 2022;235:107664.
- [12] Chen MZ, Hu Y. *Inerter and its application in vibration control systems*. Springer; 2019.
- [13] Altay O. Vibration mitigation systems in structural engineering. 2021. <http://dx.doi.org/10.1201/9781315122243>.
- [14] Cristian P, Septimiu L, Florentina C, Roşca O. Structural control systems implemented in civil engineering. *Bull Polytech Inst Jassy Construct Architect Section* 2005;LI (LV).
- [15] Constantinou MC, Soong TT, Dargush GF. *Passive energy dissipation systems for structural design and retrofit*. 1998.
- [16] Schmelzer B, Oberguggenberger M, Adam C. Efficiency of tuned mass dampers with uncertain parameters on the performance of structures under stochastic excitation. *Proc Inst Mech Eng O* 2010;224(4):297–308. <http://dx.doi.org/10.1243/1748006XJRR310>.
- [17] Wagg DJ. A review of the mechanical inerter: historical context, physical realisations and nonlinear applications. *Nonlinear Dynam* 2021;104(1):13–34.
- [18] Den Hartog JP. *Mechanical vibrations*. 4th ed.. Dover Publications. New York; 1985.
- [19] Lazar I, Neild S, Wagg D. Using an inerter-based device for structural vibration suppression. *Earthq Eng Struct Dyn* 2014;43(8):1129–47. <http://dx.doi.org/10.1002/eqe.2390>.
- [20] Bekdaş G, Nigdeli SM. Mass ratio factor for optimum tuned mass damper strategies. *Int J Mech Sci* 2013;71:68–84. <http://dx.doi.org/10.1016/j.ijmecsci.2013.03.014>.
- [21] Pietrosanti D, De Angelis M, Giaralis A. Experimental study and numerical modeling of nonlinear dynamic response of SDOF system equipped with tuned mass damper inerter (TMDI) tested on shaking table under harmonic excitation. *Int J Mech Sci* 2020;184:105762. <http://dx.doi.org/10.1016/j.ijmecsci.2020.105762>.
- [22] Pietrosanti D, De Angelis M, Basili M. Optimal design and performance evaluation of systems with tuned mass damper inerter (TMDI). *Earthq Eng Struct Dyn* 2017;46(8):1367–88. <http://dx.doi.org/10.1002/eqe.2861>.
- [23] Furtmüller T, Joas G, Adam C. Control of pendulum oscillations by tuned liquid dampers. *J Fluids Struct* 2022;114:103753. <http://dx.doi.org/10.1016/j.jfluidstruct.2022.103753>.
- [24] Ziegler F, Reiterer M. Control of vibration prone bridges by tuned liquid column dampers (TLCD). In: *Proceedings of the 12th international congress on sound and vibration 2005, ICSV 2005*, vol. 6. 2005, p. 5112–9.
- [25] Kelly JM. Base isolation: Linear theory and design. *Earthq Spectra* 1990;6(2):223–44. <http://dx.doi.org/10.1193/1.1585566>.
- [26] Ikago K, Saito K, Inoue N. Seismic control of single-degree-of-freedom structure using tuned viscous mass damper. *Earthq Eng Struct Dyn* 2012;41(3):453–74. <http://dx.doi.org/10.1002/eqe.1138>.
- [27] Zhang Z, Høeg C. Inerter-enhanced tuned mass damper for vibration damping of floating offshore wind turbines. *Ocean Eng* 2021;223:108663. <http://dx.doi.org/10.1016/j.oceaneng.2021.108663>.
- [28] Di Matteo A, Masnata C, Adam C, Pirrotta A. Optimal design of tuned liquid column damper inerter for vibration control. *Mech Syst Signal Process* 2022;167:108553. <http://dx.doi.org/10.1016/j.ymssp.2021.108553>.
- [29] Masnata C, Di Matteo A, Adam C, Pirrotta A. Assessment of the tuned mass damper inerter for seismic response control of base-isolated structures. *Struct Control Health Monit* 2021;28(2):e2665.
- [30] Masnata C, Di Matteo A, Adam C, Pirrotta A. Nontraditional configuration of tuned liquid column damper inerter for base-isolated structures. *Mech Res Commun* 2023;129:104101. <http://dx.doi.org/10.1016/j.mechrescom.2023.104101>.
- [31] Smith MC. Force-controlling mechanical device. 2002, U.S. Patent 7, 316, 303 B2.
- [32] Wang F-C, Hsu M-S, Su W-J, Lin T-C. Damping and inertial hydraulic device. 2009, U.S. Patent 2009/0108510 A1.
- [33] Gartner BJ, Smith MC. Damping and inertial hydraulic device. 2011, U.S. Patent 13/577, 234.
- [34] Wang F-C, Hsieh M-R, Chen H-J. Stability and performance analysis of a full-train system with inerters. *Veh Syst Dyn* 2012;50(4):545–71. <http://dx.doi.org/10.1080/00423114.2011.606368>.
- [35] Wang F-C, Su W-J. Inerter nonlinearities and the impact on suspension control. 2008, p. 3245–50. <http://dx.doi.org/10.1109/ACC.2008.4586992>.
- [36] Shen Y, Chen L, Liu Y, Zhang X, Yang X. Optimized modeling and experiment test of a fluid inerter. *J Vibroeng* 2016;18(5):2789–800. <http://dx.doi.org/10.21595/jve.2016.16885>.
- [37] Liu X, Jiang JZ, Titurus B, Harrison A. Model identification methodology for fluid-based inerters. *Mech Syst Signal Process* 2018;106:479–94. <http://dx.doi.org/10.1016/j.ymssp.2018.01.018>.
- [38] Swift SJ, Smith MC, Glover AR, Papageorgiou C, Gartner B, Houghton NE. Design and modelling of a fluid inerter. *Internat J Control* 2013;86(11):2035–51. <http://dx.doi.org/10.1080/00207179.2013.842263>.
- [39] Chillemi M, Furtmüller T, Adam C, Pirrotta A. Nonlinear mechanical model of a fluid inerter. *Mech Syst Signal Process* 2023;188:109986. <http://dx.doi.org/10.1016/j.ymssp.2022.109986>.
- [40] Chillemi M, Furtmüller T, Adam C, Pirrotta A. Experimental and numerical investigation of a fluid inerter for structural control. *J Sound Vib* 2024;573:118222. <http://dx.doi.org/10.1016/j.jsv.2023.118222>.
- [41] Papageorgiou C, Houghton NE, Smith MC. Experimental testing and analysis of inerter devices. *J Dyn Syst Meas Control* 2008;131(1):011001. <http://dx.doi.org/10.1115/1.3023120>.
- [42] Gonzalez-Buelga A, Lazar IF, Jiang JZ, Neild SA, Inman DJ. Assessing the effect of nonlinearities on the performance of a tuned inerter damper. *Struct Control Health Monit* 2017;24(3):e1879. <http://dx.doi.org/10.1002/stc.1879>.
- [43] Liu C, Chen L, Lee HP, Yang Y, Zhang X. A review of the inerter and inerter-based vibration isolation: Theory, devices, and applications. *J Franklin Inst B* 2022;359(14):7677–707. <http://dx.doi.org/10.1016/j.jfranklin.2022.07.030>.
- [44] Chillemi M, Furtmüller T, Adam C, Pirrotta A. Experimental and numerical study on a nonlinear fluid inerter for structural control. 2023, 18. D-A-CH-Tagung Erdbebeningenieurwesen und Baudynamik.
- [45] Kawrza M, Furtmüller T, Adam C, Maderebner R. Parameter identification for a point-supported cross laminated timber slab based on experimental and numerical modal analysis. *Eur J Wood Wood Prod* 2021;79. <http://dx.doi.org/10.1007/s00107-020-01641-7>.
- [46] Gao H, Wang H, Li J, Wang Z, Liang R, Xu Z, et al. Optimum design of viscous inerter damper targeting multi-mode vibration mitigation of stay cables. *Eng Struct* 2021;226:111375.
- [47] Zhu C, Yang J, Rudd C. Vibration transmission and power flow of laminated composite plates with inerter-based suppression configurations. *Int J Mech Sci* 2021;190:106012. <http://dx.doi.org/10.1016/j.ijmecsci.2020.106012>, URL <https://www.sciencedirect.com/science/article/pii/S0020740320313345>.
- [48] Chillemi M, Furtmüller T, Adam C, Pirrotta A. Assessing the effect of different configurations of inerter-based devices for structural vibration control. In: *Proceedings of the 16th international conference on dynamical systems. theory and applications*, vol. 2. 2021, p. 205–6.

- [49] Furtmüller T, Di Matteo A, Adam C, Pirrotta A. Base-isolated structure equipped with tuned liquid column damper: An experimental study. *Mech Syst Signal Process* 2019;116:816–31. <http://dx.doi.org/10.1016/j.ymssp.2018.06.048>.
- [50] Brown P, McPhee J. A continuous velocity-based friction model for dynamics and control with physically meaningful parameters. *J Comput Nonlinear Dyn* 2016;11(5). <http://dx.doi.org/10.1115/1.4033658>.
- [51] Liu X, Titurus B, Jiang JZ. Generalisable model development for fluid-inerter integrated damping devices. *Mech Mach Theory* 2019;137:1–22.
- [52] Brzeski P, Kapitaniak T, Perlikowski P. Novel type of tuned mass damper with inerter which enables changes of inertance. *J Sound Vib* 2015;349:56–66.
- [53] Vold H, Crowley J, Rocklin GT. New ways of estimating frequency response functions. *Sound Vib* 1984;18(11):34–8.
- [54] Roberts JB, Spanos PD. *Random vibration and statistical linearization*. Wiley; 1991.
- [55] Di Paola M, Navarra G. Stochastic seismic analysis of MDOF structures with nonlinear viscous dampers. *Struct Control Health Monit* 2009;16(3):303–18. <http://dx.doi.org/10.1002/stc.254>.
- [56] Di Matteo A, Iacono FL, Navarra G, Pirrotta A. Direct evaluation of the equivalent linear damping for TLCD systems in random vibration for pre-design purposes. *Int J Non-Linear Mech* 2014;63:19–30.
- [57] Brandner R, Flatscher G, Ringhofer A, Schickhofer G, Thiel A. Cross laminated timber (CLT): overview and development. *Holz als Roh- und Werkstoff* 2016;74. <http://dx.doi.org/10.1007/s00107-015-0999-5>.
- [58] Kurzinski S, Crovella P, Kremer P. Overview of cross-laminated timber (CLT) and timber structure standards across the world. *Mass Timber Construct J* 2022;5(1):1–13.
- [59] Piersol AG, Paez TL. *Harris' shock and vibration handbook-Effects of shock and vibration on humans*. McGraw-Hill, New York; 2010.
- [60] Brandt A. *Noise and vibration analysis: signal analysis and experimental procedures*. John Wiley & Sons; 2023.
- [61] Kawrza M, Furtmüller T, Adam C. Experimental and numerical modal analysis of a cross laminated timber floor system in different construction states. *Constr Build Mater* 2022;344:128032. <http://dx.doi.org/10.1016/j.conbuildmat.2022.128032>.
- [62] Kim YR, Kim K-J. Indirect input identification by modal model technique. In: *Proceedings of the 15th international modal analysis conference*, vol. 3089. 1997, p. 1263.
- [63] Lang GF, Snyder D, et al. Understanding the physics of electrodynamic shaker performance. *Sound Vibr* 2001;35(10):24–33.
- [64] Zangwill A. *Modern electrodynamics*. Cambridge University Press; 2012, <http://dx.doi.org/10.1017/CBO9781139034777>.
- [65] Lagarias JC, Reeds JA, Wright MH, Wright PE. Convergence properties of the nelder–mead simplex method in low dimensions. *SIAM J Optim* 1998;9(1):112–47.
- [66] Ewins DJ. *Modal testing: theory, practice and application*. John Wiley & Sons; 2009.
- [67] Preumont A. *Vibration control of active structures*, vol. 2, Springer; 1997.
- [68] Warburton G. Optimum absorber parameters for minimizing vibration response. *Earthq Eng struct Dyn* 1981;9(3):251–62.
- [69] CEN, Comité Européen de Normalisation, et al. *Eurocode 5—Design of timber structures*. 1995.